ASSESSING POTENTIAL OF UAV MULTISPECTRAL IMAGERY FOR ESTIMATION OF AGB AND CARBON STOCK IN CONIFER FOREST OVER UAV RGB IMAGERY

KEZANG GADEN
JUNE, 2020

SUPERVISORS:
dr. Y.A. Hussin
ir L.M. van Leeuwen - de Leeuw

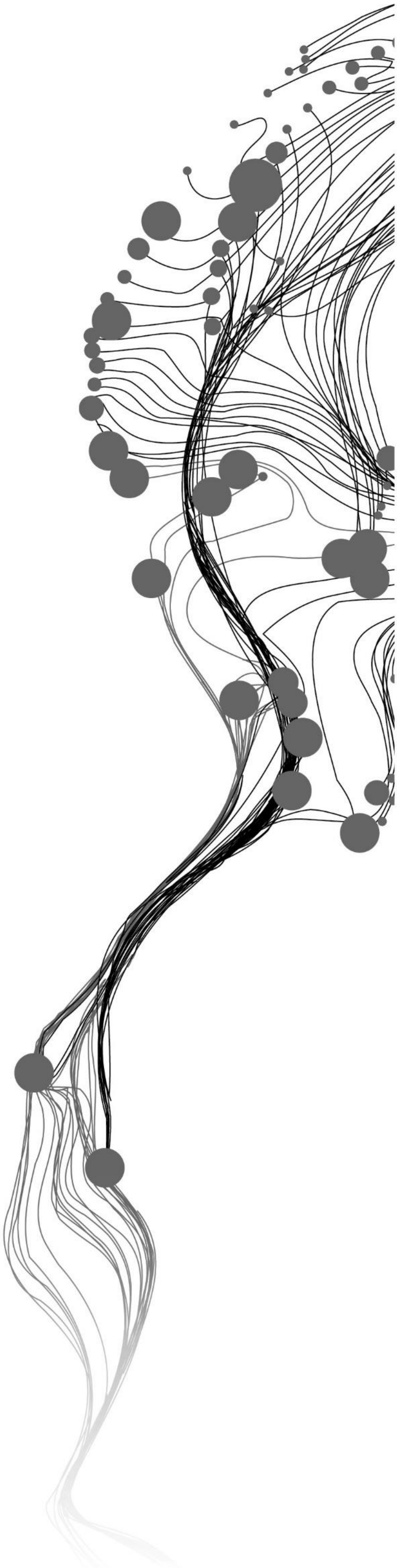

ASSESSING POTENTIAL OF UAV MULTISPECTRAL IMAGERY FOR ESTIMATION OF AGB AND CARBON STOCK IN CONIFER FOREST OVER UAV RGB IMAGERY

KEZANG GADEN
Enschede, The Netherlands, June, 2020

Thesis submitted to the Faculty of Geo-Information Science and Earth Observation of the University of Twente in partial fulfilment of the requirements for the degree of Master of Science in Geo-information Science and Earth Observation.
Specialization: Natural Resources Management

SUPERVISORS:
dr. Y.A. Hussin
ir L.M. van Leeuwen - de Leeuw

THESIS ASSESSMENT BOARD:
dr. A.G. Toxopeus (Chair)
dr. T.L.U. Kauranne (External Examiner, Lappeenranta University of Technology, Finland)

ABSTRACT

The information on forest biomass and carbon stock is essential to monitor and report national greenhouse gas (GHG) inventories to UNFCCC. Forestry is one of the crucial sectors in a national GHG inventory as deforestation and forest degradation is the second critical drivers of climate change. Conifer forest plays a vital role in the global carbon cycle by sequestering carbon dioxide from the atmosphere due to its fast growth. Field-based inventory and remote sensing (RS) are both recommended by UNFCCC to assess forest biomass and carbon stock for REDD+. RS method is considered to be more efficient over the costly traditional forest inventory for large scale assessments. Among widely available remote sensing data, UAV images allow retrieving individual tree parameters owing to its high image resolution. Studies have found UAV RGB imagery suitable for estimating aboveground biomass or carbon (AGB/AGC) required for reporting emissions related to changes in forest biomass. However, there is hardly any study on estimation of AGB/AGC using UAV multispectral (MS) imagery with structure from motion (SfM) technique. UAV MS imagery with the high spectral resolution is expected to model DBH and estimate AGB/AGC better than UAV RGB imagery. Therefore, this study aims to evaluate the potential of UAV MS imagery to estimate AGB/AGC over the UAV RGB imagery in a part of temperate conifer forest.

The study was conducted in Snippert forest of west Lonneker, The Netherlands. Diameter at breast height (DBH) and tree height of 650 trees were measured in 35 plots selected based on simple random sampling method. UAV MS images were obtained from Parrot Sequoia MS sensor, while UAV RGB images were obtained from Phantom 4 RGB camera and processed using SfM technique in Pix4Dmapper. MS and RGB-based crown diameter were derived from canopy projection area to model DBH, and their relationship was assessed. UAV MS and RGB tree height were derived from the respective canopy height model, and their accuracies were assessed using LiDAR tree height obtained from Actueel Hoogtebestand Nederland (AHN). Regression models were compared to determine how accurately the DBH can be estimated using UAV-derived parameters. For regression models, field-measured DBH was used as a dependent variable and UAV-derived parameters such as tree height, canopy projection area, crown diameter and the combination of tree height and crown diameter as independent variables. The accuracy of the estimated DBH was evaluated using validation dataset from field-measured DBH. A species-specific allometric equation was used to estimate UAV-based AGB/AGC and compared with field LiDAR-based AGB/AGC.

A set of orthomosaic, DSM and DTM were generated from respective UAV MS and RGB images. The study found a strong positive correlation (r = 0.98) between UAV MS and RGB-derived crown diameter, indicating the suitability of retrieving crown diameter from UAV MS imagery to estimate DBH. UAV MS-derived tree height (R^2 = 0.79) was slightly less accurate than UAV RGB-derived tree height (R^2 = 0.83). However, a higher deviation was observed in RGB-derived tree height (RMSE = 2.95 m) compared to MS-derived tree height (RMSE = 1.94 m) which is attributed to a high spatial resolution of UAV RGB images. Quadratic model of both MS and RGB showed the higher model performance to predict DBH. Using validation dataset, MS model (R^2 = 0.82; RMSE = 4.36 cm) estimated DBH more accurate than RGB model (R^2 = 0.80; RMSE = 4.53 cm). Mean AGB assessed from the field with LiDAR-measured parameter was 8.49 Mg plot^{-1} (i.e. 169.83 Mg ha^{-1}). In contrast, the mean AGB estimated from UAV MS and RGB imagery was 8.68 and 9.06 Mg plot^{-1} (i.e. 173.52 and 181.24 Mg ha^{-1}), respectively. As expected, the accuracy of AGB estimated from MS-derived parameters (R^2 = 0.91; RMSE = 149.71 kg) was higher than RGB-derived parameters (R^2= 0.89; RMSE = 166.85 kg), which is explained by higher accuracy of DBH modelled from MS-derived parameters. Therefore, this study concludes that UAV MS imagery is suitable to estimate AGB/AGC, and performs better than UAV RGB imagery suggesting a promising application for REDD+ monitoring and forest management practices in a managed coniferous forest at a local scale.

Keywords: AGB, AGC, UAV, Multispectral, SfM, CHM

ACKNOWLEDGEMENTS

I would like to express my sincere gratefulness to Tripple Gem for showering me with invaluable blessings at all times. My heartfelt gratitude goes to Orange Knowledge Programme (OKP), NUFFIC, for granting me a scholarship to study in ITC, University of Twente. If not for this opportunity, it would not have been possible for me to come to The Netherlands and study as an international student.

My genuine and most profound gratitude goes to dr. Y.A. Hussin and ir L.M. van Leeuwen - de Leeuw for being an inspiring supervisor. This study would not have completed without their guidance and persistent help. My sincere appreciation goes to dr. A.G. Toxopeus, chair of thesis assessment board, for his constructive feedbacks during the proposal defence and mid-term presentation, and drs. R.G. Nijmeijer, NRM course director, for coordinating the overall course and particularly the MSc research.

My appreciation goes to Bureau Takkenkamp for granting permission to fly a drone and conduct fieldwork in the study area. I would like to thank T.M.R. Roberts, ITC drone expert, for collecting the UAV data for this study, and C. Marcatelli, ITC education and research technician, for providing training on the use of GNSS. Also, my gratitude goes to A.S. Masselink (Benno), ITC education and research technician, for providing the necessary equipment for thesis fieldwork.

I extend my earnest thanks to drs. E.H. Kloosterman, Faculty to NRS, and dr. P. Nyktas, Faculty to NRS, for their advice and suggestions. I am much thankful to my classmate, W.A. Worku and M.A. Eshetae for their immense help in collecting the ground-truth data.

My appreciation also goes to Sherubtse College, Royal University of Bhutan, for granting me the study leave and rendering necessary help whenever required.

Last but not least, my deepest gratefulness goes to my family, parents, and friends for their love and immense support. I am sorry for being unable to mention the individual names, but the help and assistance rendered to me throughout the study period shall always remain in my heart.

Kezang Gaden
June 2020
Enschede

TABLE OF CONTENTS

LIST OF FIGURES

LIST OF TABLES

ACRONYMS

AHN	Actueel Hoogtebestand Nederland
AGB	Aboveground biomass
AGC	Aboveground carbon
ALS	Airborne Laser Scanning
ANOVA	Analysis of variance
C	Carbon
CD	Crown diameter
CF	Conversion factor
CHM	Canopy Height Model
CO_2	Carbon dioxide
CPA	Canopy Projection Area
DBH	Diameter at breast height
DSM	Digital Surface Model
DTM	Digital Terrain Model
GCP	Ground control point
GHG	Greenhouse gas
GNSS RTK	Global Navigation Satellite System Real-time Kinematic
GSD	Ground sampling distance
Ha	Hectare
IUCN	International Union for the Conservation of Nature
Kg	Kilogram
LiDAR	Light Detection and Ranging
Mg	Megagram
MRV	Measurement, Reporting, and Verification
MS	Multispectral
NDVI	Normalised Difference Vegetation Index
NIR	Near-infrared
RADAR	Radio Detection and Ranging
REDD	Reducing Emissions from Deforestation and Forest Degradation
RGB	Red Green Blue
RMSE	Root Mean Square Error
RS	Remote sensing
SDGs	Sustainable Development Goals
SfM	Structure from Motion
TH	Tree height
UAS	Unmanned Aerial System
UAV	Unmanned Aerial Vehicle
UNFCCC	United Nations Framework Convention on Climate Change
VHR	Very high-resolution

1. INTRODUCTION

1.1. Conifer forest

Conifers forest dominantly consist of evergreen cone-bearing woody trees with scale-like leaves and cone shape canopies. Forest in the boreal and temperate climate zones are almost entirely of conifers, covering a vast area of land in North America, Europe, Asia, and other places with mountain ecosystems. There are some 615 species of conifer in total, including 41 species in Europe with common species such as Norway spruce, Scots pine, and Douglas fir (Farjon, 2018). Conifers are the largest community of gymnosperm with a unique shoot and canopy structure having various ecological and economic significance. They play a major part in the global carbon cycle (Houghton et al., 2009) by sequestering carbon dioxide (CO_2) from the atmosphere through photosynthesis during growth and storing them in their leaves, branches, trunks, and roots for many years (Toochi, 2018). Thurner et al. (2014) reported higher carbon density in a temperate conifer forest (6.21 ± 2.07 kg C m^{-2}) compared to temperate broadleaf/mixed forest (5.80 ± 2.21 kg C m^{-2}) and boreal forest (4.00 ± 1.54 kg C m^{-2}). Apart from carbon sequestration, conifers provide habitat for a wide range of terrestrial animals species. The fast growth and its wood properties make conifers a leading source of industrial wood (Farjon, 2018). Europe has 15% of the total exploitable conifer forest area and growing stock of the world. However, they account for 25% of the total industrial wood production (Cooper, 2003). The large share of industrial wood production with increasing demand for consumption of a wood product instigate forest degradation. The annual report of International Union for the Conservation of Nature (IUCN) Red List of Threatened Species published in 2013 noted that conifers are declining and 34% of all conifer species are threatened with extinction (IUCN, 2013) due to logging and other human activities (Farjon, 2018). Therefore conservation of conifers is vital to ensure sustainable use of its ecosystem services.

1.2. Need to estimate AGB/AGC

Biomass is the amount of plant material expressed as oven-dry mass per unit area obtained through photosynthesis (McKendry, 2002). The aboveground biomass (AGB) comprises of the leaf, branch, and stem biomass above the soil (IPCC, 2003). Generally, carbon accounts for half of the biomass (Hirata et al., 2012). Information on forest biomass and carbon stock is crucial for international climate policies, and conservation programs targeting for mitigation of global climate change. AGB has been regarded as one of the terrestrial essential climate variables of the Global Climate Observing System (GCOS) (Duncanson et al., 2019; Herold et al., 2019). Countries that are parties to climate change convention is obliged to report national greenhouse gas (GHG) inventories both at sources and sinks to the United Nations Framework Convention on Climate Change (UNFCCC). Forestry is one of the important sectors in a national GHG inventory as deforestation and forest degradation is the second critical drivers of climate change after the energy sector, which approximately shares 17% of total carbon emissions (IPCC, 2007). Accurate and periodically updated information on forest cover, AGB and carbon stock are essential for conservation programs, including Reducing Emissions from Deforestation and Forest Degradation (REDD) to the UNFCCC. Through the REDD program, countries will receive economic benefits for enhancing forest conservation, forested carbon stocks, and sustainable management of the forest (REDD+). However, the achievements of REDD+ will depend on having a robust method that is reasonably accurate, cheap, operational, and technically easy for measurement, reporting, and verification (MRV) system. MRV of carbon stock and its alteration over time for a country is indispensable to ensure that the financial remuneration for the reduction in carbon emission is evidence-based and transparent (Gibbs et al., 2007).

1.3. Challenges in estimating AGB/AGC

Remote sensing (RS) technology is much used in forestry to retrieve forest parameters (McRobert & Tomppo, 2007; Mlambo et al., 2017). RS has the advantage of acquiring spatial data over a larger area that is not accessible by traditional field survey. However, most of the RS data are not suitable for estimating AGB/AGC accurately. For instance, optical RS is limited by the presence of cloud, illumination effect, and its ability to capture images only during daylight (Rodríguez-Veiga et al., 2017). Low and moderate-resolution optical data (e.g. MODIS) are less accurate and not viable for the estimation of carbon stock at a plot level (Baccini et al., 2008). The very high-resolution (VHR) image (e.g. QuickBird) are costly and often not available for all regions (Rodríguez-Veiga et al., 2017). An alternative method to address the limitations of optical RS is to use active RS such as Radio Detection and Ranging (RADAR) and Light Detection and Ranging (LiDAR). However, RADAR has dense canopy saturation (Huang et al., 2018), especially C-band, apart from technical complexities to process the data and relatively low spatial resolution. Although dense point cloud generated from LiDAR is feasible to measure tree height and crown size at tree level, airborne laser scanning (ALS) is a single time operation and costly to use (Gibbs et al., 2007; Mlambo et al., 2017). Thus, an accurate estimation of forest biomass and carbon stock necessitates cost-effective high spatial and temporal resolution of data to circumvent such issues. In this regard, Unmanned aerial vehicle (UAV) has a higher possibility of addressing most of the identified challenges.

1.4. Advantage of UAV

UAV, also known as the unmanned aerial system (UAS) or drone is a type of an aircraft that can be controlled remotely and fly without a pilot on-board. It consists of three major elements; the unmanned aircraft, the ground control station and the communication to command and control the aircraft (Colomina & Molina, 2014). It is fast emerging low altitude RS increasingly used to collect data in forestry (Puliti et al., 2015; Torresan et al., 2017) as it has an advantage of retrieving information of the same area more frequently due to its mobilisation flexibility and handy to use. They can fly relatively at low altitude, collecting very high spatial resolution data to retrieve forest parameters at both stand and tree level (Grznárová et al., 2019; Guerra-Hernández et al., 2017; Lin et al., 2018; Mlambo et al., 2017; Puliti et al., 2015; Zhang et al., 2016) over a small area with minimal expense. At the same time, the availability of powerful photogrammetric software with Structure from Motion (SfM) technique provides the flexibility of processing large geospatial datasets making both data collection and processing a cost-effective alternative for various forestry application. Studies have demonstrated the capability of UAV RGB images with SfM technique (Mohan et al., 2017) in retrieving tree parameters such as crown size and tree height in a relatively sparse forest and indicated the potentiality to estimate AGB and carbon stock (Guerra-Hernández et al., 2016; Wallace et al., 2016). The disadvantage of UAV is the lack of global coverage due to limited battery life, and surveying large areas like satellites and aircraft would require a hybrid UAV which is costly. Nevertheless, they are much cheaper than aircraft for local use, especially in developing countries. After using UAV for 20-30 times, their cost would become almost a few Euros.

1.5. Assessment of AGB/AGC using UAV RGB imagery

Among different sensors mounted for use on the UAV platform, RGB camera is one of the most commonly used sensors at present to estimate AGB (Guerra-Hernández et al., 2017; Lin et al., 2018; Messinger et al., 2016) and carbon stock in both tropical and temperature forest with reasonable accuracy. Both parametric and non-parametric methods are used to estimate forest biomass using remotely sensed data. The parametric approach includes regression-based models while non-parametric approaches are an artificial neural network, random forest, and support vector machine, to name a few among others (Kachamba et al., 2016). For instance, Lin et al. (2018) used the non-linear regression model to estimate AGB using UAV CHM-derived tree height as a predictor. González-Jaramillo et al. (2019) used CHM to predict DBH using a height diameter relationship equation, and estimate AGB, while Ota et al. (2015) regressed reference AGB against the CHM generated from UAV, LiDAR and their combination to fit the model and estimate the AGB (Ota et al., 2015). Kachamba et al. (2016) used multiple regression model to estimate biomass using the canopy height, canopy density, and spectral variables obtained from the RGB spectral bands. Although RGB spectral bands are used as a predictor to estimate biomass, it is limited to the visible spectrum of electromagnetic radiation. Also, its products are less sensitive to vegetation characterisation processes, unlike the multispectral sensor. Some consumer-grade photography cameras can be modified using filters to obtain near-infrared (NIR) data (Lehmann et al., 2015), but the result from such data is complicated to interpret. Therefore, obtaining the right data is essential to achieve a meaningful result.

1.6. Potential of UAV MS imagery to estimate AGB/AGC

Multispectral images can be obtained by Sequoia multispectral sensor fixed on the UAV platform. Sequoia has two imbedded cameras to capture images in both visible and NIR wavelength: i) RGB camera (16-megapixel rolling shutter) to capture images in red, green, blue waveband, and ii) Multispectral camera (1.2-megapixel monochrome global shutter) to capture images in green (central wavelength: 550nm; bandwidth: ± 40nm), red (660nm; ± 40nm), red edge (735nm; ± 10nm) and near-infrared (790nm; ± 40nm) wavebands. The multispectral camera has a focal length of 4 mm with horizontal, vertical, and diagonal field of views of 70.6°, 52.6° and 89.6°, respectively (Cardil et al., 2019). Over the years, the use of multispectral imagery is increasing with much of its application focused on precision agriculture (Tsouros et al., 2019). In forestry, it has been used to estimate AGB (González-Jaramillo et al., 2019), monitor forest health (Dash et al., 2018; Lehmann et al., 2015), quantify defoliation (Cardil et al., 2019), evaluate forest fire severity (Carvajal-Ramírez et al., 2019), survey postfire vegetation area (Fernández-Guisuraga et al., 2018), estimate phytovolume (Carvajal-Ramírez et al., 2019), classify tree species (Gini et al., 2014), and map coastal dune vegetation (Suo et al., 2019).

Multispectral images from the UAV platform can be used to acquire very high-resolution images to retrieve tree parameters. Multispectral images with high spectral resolution compared to RGB images is expected to perform better in delineating tree crown and modelling DBH. Nevertheless, the lower spatial resolution of MS imagery can result in low point cloud density affecting the accuracy of tree height. Since the influence of DBH is more pronounced than tree height in estimating AGB using an allometric equation, MS-derived tree parameters may perform better in estimating AGB/AGC. Shen et al. (2019) have found that multispectral point cloud and imagery derived structural and spectral matrics (R^2 = 0.62-0.73) better in predicting forest structural attributes compared to RGB point cloud and imagery derived spectral and structural matrics (R^2 = 0.56-0.64). Although not explored in this study, vegetation indices (e.g. NDVI), which can be generated from multispectral imagery is often used as variables to estimate the AGB (López-Serrano et al., 2016; Zhu & Liu, 2015).

1.7. Approach to estimate AGB/AGC

There are several methods to estimate AGB/AGC. Field-based inventory and RS are both recommended by UNFCCC to assess forest biomass and carbon stock for REDD+ (Hirata et al., 2012). A typical non-destructive way to estimate forest biomass is using an allometric equation (Kumar & Mutanga, 2017). Generally, diameter at breast height (DBH) and tree height are the key input to estimate AGB using an allometric equation. Tree height can be measured either indirectly from UAV imagery using SfM or directly through LiDAR. However, the stem diameter cannot be measured directly from remote sensing imagery. Tree parameters, such as tree height (TH) (González-Jaramillo et al., 2019), crown diameter (CD) (Berhe, 2018; Hashem, 2019; Kustiyanto, 2019; Odia, 2018; Shah, 2011), and their combination (Guerra-Hernández et al., 2017; Heurich et al., 2004; Jucker et al., 2017; Popescu, 2007; Zhao et al., 2009) retrieved from remotely sensed data are being used to estimate DBH using an either parametric or non-parametric approach. The accuracy of parameters obtained from UAV imagery can be assessed by non-destructive field measurement.

In this research, crown diameter and tree height derived from UAV MS imagery were first used to model DBH. The predicted DBH and tree height was then used as an input to estimate AGB/AGC using the species-specific allometric equation. The UAV-derived parameters were compared with field and LiDAR-based reference parameter using linear regression to assess their accuracies and applicability for forest management and REDD+ monitoring. The information on AGB/AGC is particularly crucial for REDD+ and conservation of the forest ecosystem. The REDD+ is a proposal to offer economic incentives to encourage countries to reduce deforestation and forest-related CO_2 emissions below the set baseline. Since REDD+ is planned to kick-start its implementation phase by 2020, there is a need to identify a robust method for MRV, which UAV MS imagery with SfM technique may provide. The key concepts, approach, and application are shown in *Figure 1*.

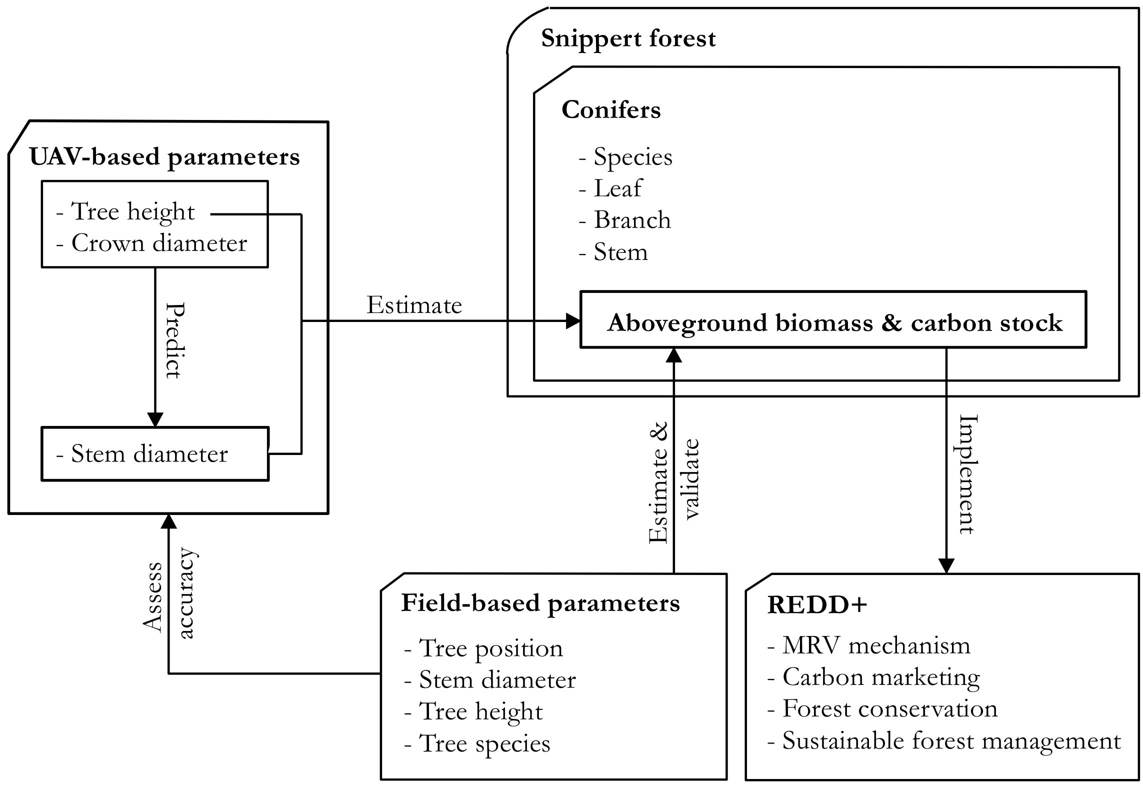

Figure 1. Conceptual diagram.

1.8. Problem statement

Monitoring forest biomass and carbon stock is crucial for REDD+, conservation and sustainable management of forest resources. For ages, assessment of forest biomass has relied on the classical forest inventory data despite being expensive, time-consuming and datasets often limited to a small area (Balsi et al., 2018; Fehrmann & Kleinn, 2006; Pouliot et al., 2002). Remote sensing method is considered to be more efficient for large scale assessment that is inaccessible by traditional field survey. Among remotely sensed data, UAV images have provided a cost-effective technique to retrieve both the 2D and 3D information even at tree level (McRobert & Tomppo, 2007; Mlambo et al., 2017). Very high-resolution orthophoto generated from UAV RGB imagery is used to delineate canopy projection area (CPA) to model DBH. However, delineating tree crowns using UAV RGB images are challenging, especially in an intermingling tree crowns with mixed tree species. Inaccurate delineation of the tree canopy can affect the accuracy of DBH prediction, which often has more influence on the estimation of AGB using a non-destructive allometric equation. Since UAV MS imagery has been reported to have a high spatial agreement of crown delineation (Cardil et al., 2019), the accuracy of DBH prediction from the crown diameter needs to be explored. Tree height is another parameter retrieved from the Canopy Height Model (CHM) produced from the Digital Surface Model (DSM) and Digital Terrain Model (DTM) using SfM technique. Accuracy of tree height depends on the accuracy of DTM (Kachamba et al., 2016; Ota et al., 2015). Studies have found UAV-derived DTM in a dense forest canopy less accurate as a passive sensor can hardly detect the forest floor. Moreover, the UAV images acquired from a different sensor with different image resolution may affect the output of DSM and DTM due to difference in point cloud density. Therefore, assessing the accuracy of tree height derived from the multispectral sensor and RGB camera is crucial to determine the margin of error in tree height estimation.

To the knowledge of this research, the MS sensor has hardly been applied in temperate conifer forest to retrieve tree parameters despite its potentiality to acquire a very high-resolution image. González-Jaramillo et al. (2019) have used UAV MS imagery to estimate AGB from Normalised Difference Vegetation Index (NDVI) using an equation and found less accurate due to the saturation effect of dense canopy compared to UAV RGB imagery using the SfM photogrammetric approach. Nevertheless, the estimation of AGB/AGC from UAV MS imagery using the SfM technique and its comparison with UAV RGB imagery is hard to find in literature. Thus, there is a need to assess the potential of tree parameters extracted from UAV MS imagery to estimate AGB/AGC. This research hypothesises that the estimation of AGB/AGC using UAV MS imagery would be more accurate than UAV RGB imagery. Therefore, this study aims to address the research gap relating to the potentiality of UAV MS imagery in retrieving tree crown diameter and tree height to estimate AGB/AGC using the SfM technique as a possible alternative for REDD+ monitoring and sustainable management of the forest.

1.9. Research objective

1.9.1. Main objective

To evaluate the accuracy of estimating AGB/AGC in part of a temperate European conifer forest using multispectral senor imagery over the RGB imagery of UAV platform.

1.9.2. Specific objective

1. Assess the relationship between UAV MS-derived and UAV RGB-derived tree crown diameter.
2. Assess the accuracy of tree height derived from CHM of UAV MS and RGB imagery.
3. Model tree DBH using the crown diameter and tree height from UAV MS and RGB imagery.
4. Estimate AGB/AGC from UAV MS, and RGB imagery.
5. Compare the accuracy of AGB/AGC estimated from UAV MS and RGB imagery.

1.10. Research question

1. What is the correlation between the tree crown diameter obtained from UAV MS and RGB imagery?
2. How accurate is the tree height obtained from CHM of UAV MS and RGB imagery?
3. How accurate is the DBH predicted using the crown diameter and tree height as a compound variable from UAV MS and RGB imagery?
4. What is the AGB/AGC estimated from UAV MS and RGB imagery?
5. How accurate is the AGB/AGC estimated from UAV MS and RGB imagery?

1.11. Hypothesis

1. H0: Tree crown diameter estimated from UAV MS, and RGB imagery has no significant difference.
   H1: Tree crown diameter estimated from UAV MS, and RGB imagery has a significant difference.
2. H0: UAV MS and RGB-estimated tree height, and LiDAR-measured tree height have no significant difference.
   H1: UAV MS and RGB-estimated tree height, and LiDAR-measured tree height have a significant difference.

3. H0: DBH predicted from UAV MS, and RGB-derived parameters and DBH measured in the field has no significant difference.
   H1: DBH predicted from UAV MS, and RGB-derived parameters and DBH measured in the field has a significant difference.
4. H0: AGB estimated from UAV MS, and RGB-derived parameters and field with LiDAR-measured parameter have no significant difference.
   H1: AGB estimated from UAV MS, and RGB-derived parameters and field with LiDAR-measured parameter have a significant difference.
5. H0: AGB estimated from UAV-derived parameters and field with LiDAR-measured parameter has no significant relationship.
6. H1: AGB estimated from UAV-derived parameters and field with LiDAR-measured parameter has a significant relationship.

2. MATERIAL AND METHOD

2.1. Study area

Snippert forest is located in west Lonneker (52°16'17.4"N, 6°57'18.63"E), eight-kilometres northeast of Enschede (*Figure 2*). The total forest is approximately 1 × 2 km including Haagse Bos forest managed by the natural monument. Snippert forest is a semi-natural forest managed by a private company (Bureau Takkenkamp) for timber production. The study area covers 30 ha (0.3 km²) with two dominant conifer species, Norway spruce (*Picea abies*) and Scots pine (*Pinus sylvestris*). The area is relatively flat with an altitude ranging from 46 to 52 m above mean sea level. The climate is warm in summer with an average monthly temperature ranging from 12°C to 25°C (KNMI, 2019), while winter remains very cold and windy with temperature even below zero.

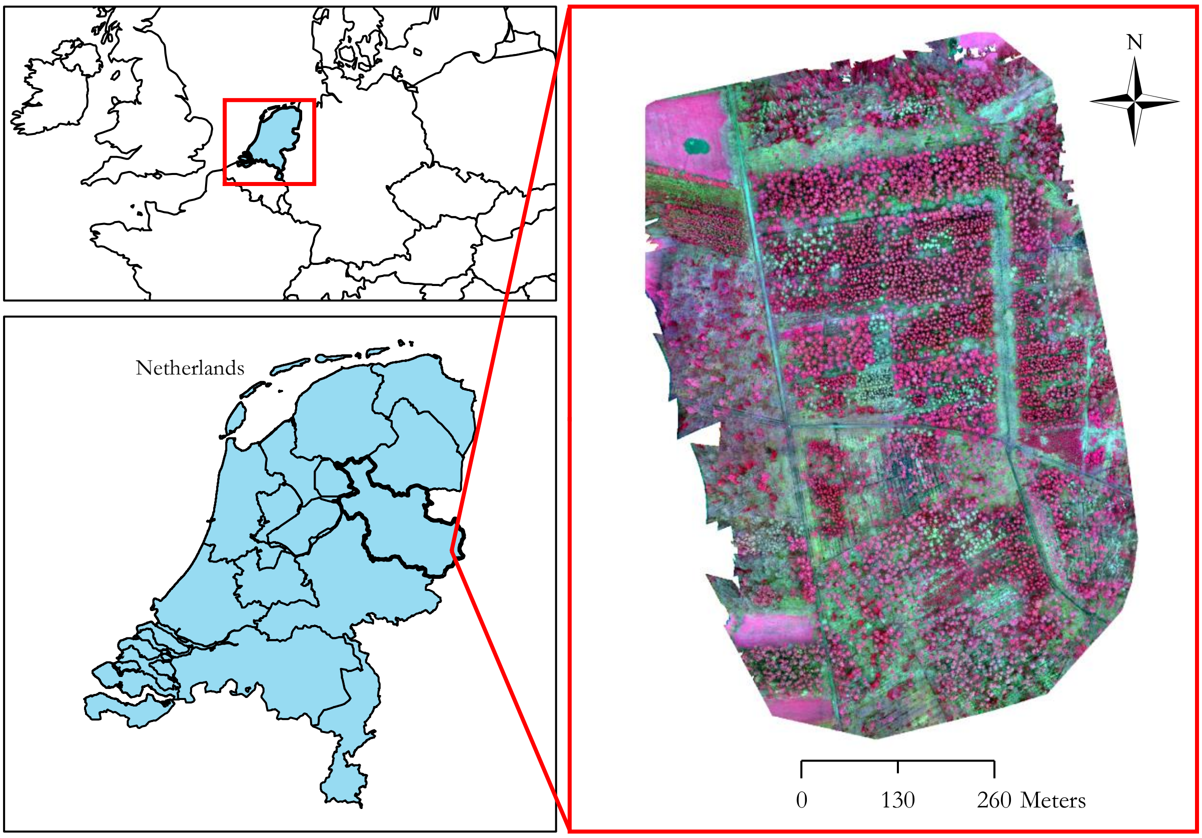

Figure 2. Location map of the study area.

2.2. Material

This section includes data, equipment, and software. The data was collected using equipment in the field and processed using various software packages.

2.2.1. Data

This study used both UAV imagery and plot data collected during the fieldwork. The UAV data consists of MS and RGB images acquired using Parrot Sequoia multispectral sensor and RGB camera, respectively. The ground control points (GCPs) were distributed before the UAV flight and measured later. The plot data comprises of tree parameters measured during the fieldwork (*Table 1*).

Table 1. Data and sources.

Data	Source
Coordinate of sample plot centre	Global navigation satellite system real-time kinematic (GNSS RTK)
Diameter at breast height (DBH)	Fieldwork
Tree height	Fieldwork
Coordinate of trees in sample plot	Fieldwork
Species	Fieldwork
UAV MS images	Parrot Sequoia multispectral sensor
UAV RGB images	Phantom 4 RGB camera
Ground control points (GCPs)	GNSS RTK
LiDAR data	Actueel Hoogtebestand Nederland (AHN)

2.2.2. Equipment

The equipment listed in *Table 2* were used to collect data during the fieldwork. It includes both field-based and UAV-based tools required to acquire primary data for this study.

Table 2. Field equipment and purpose.

Equipment	Use
Tree tag	Number trees
Diameter tape	Measure DBH
Distometer (Leica DISTO)	Measure the distance of each tree from the plot centre, and measure tree height of each tree within the plot.
Clinometer (Suunto compass)	Measure bearing of each tree from the plot centre
Digital camera	Take pictures
Data collection sheet	Record tree height, DBH, coordinate, distance, bearing, and trees species
Stationery	Record field data
DJI Phantom 4 with attached Parrot Sequoia multispectral sensor	Acquire UAV MS images
AIRINOV target	Calibrate (radiometric) multispectral sensor
DJI Phantom 4	Acquire UAV RGB images
GNSS RTK	Measure coordinates of plot centre, and GCPs
GCP markers	Mark GCPs

2.2.3. Software

After the collection of data, the next task was to process and analyse the data. The data processing, analysis, and report writing were done using the software listed in *Table 3*.

Table 3. Software and purpose.

Software	Use
UgCs	UAV MS flight planning and real-time monitoring of the drone
Pix4DCapture & Pix4D Ctrl+DJI	UAV RGB flight planning and real-time monitoring of the drone
Pix4Dmapper	UAV image processing
ERDAS IMAGINE	Image processing
ArcMap	Spatial data analysis
Microsoft Excel	Data storage and analysis
R and RStudio	Data analysis
SPSS	Data analysis
Microsoft Word	Report writing
Mendeley Desktop	Citation and references
Microsoft PowerPoint	Thesis presentation

2.3. Method

Figure 3 shows the methodological steps of this research. It consists of five major parts:

i) Firstly, UAV flight planning and fieldwork planning were prepared before the actual collection of data.

ii) Secondly, UAV images were acquired and processed to generate DSM, DTM, and orthomosaic.

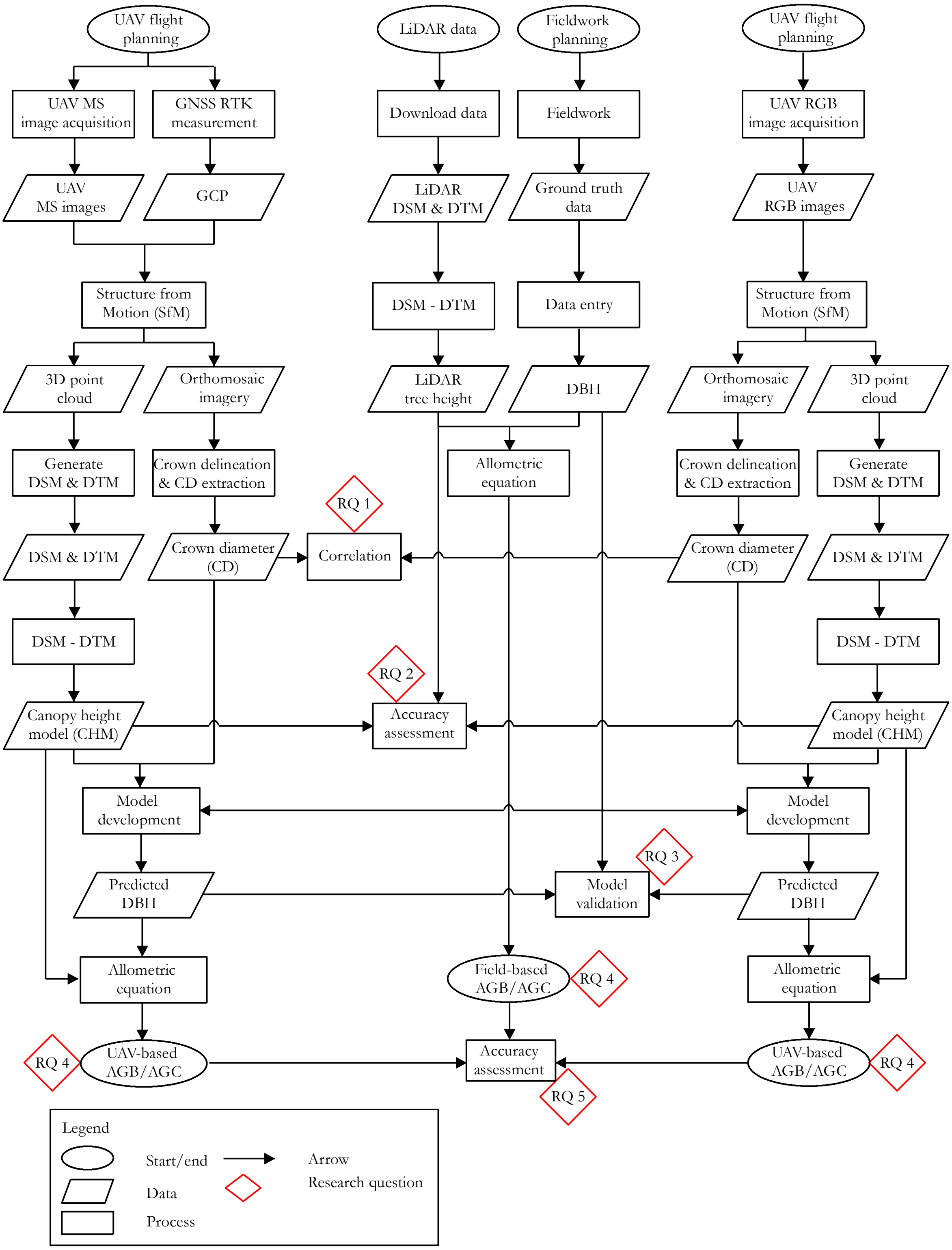

Figure 3. Flowchart of research methods.

iii) Thirdly, ground-truth data were collected and entered in Microsoft Excel for each sample plot for the analysis.
iv) Fourthly, tree crown size and tree height were extracted from orthomosaic and CHM, respectively to predict DBH.
v) Finally, tree parameters were used to estimate AGB/AGC. These five steps are elaborated in *Section 2.4 – 2.7*.

2.4. Fieldwork planning

Several issues were considered before the onset of ground-truth data collection, such as UAV flight planning, and sampling design.

2.4.1. UAV flight planning

Flight planning was prepared before the mission to ensure that the desired area is surveyed (*Figure 5a*). The flight plan parameters were set using UgCS and Pix4Dcapture application to acquire UAV MS and RGB images, respectively (*Table 4*).

Table 4. UAV flight parameters.

Parameters	Multispectral	RGB
Sensor	Parrot Sequoia multispectral	Phantom 4 RGB camera
Type of mission	Two single grid mission (North-South and East-West)	Two single grid mission (North-South and East-West)
Speed	Slow	Slow
Angle of the camera	90° (vertical)	80° (vertical)
Overlap	80 %	90 % front- and 80 % side overlap
Flight height	North-South (NS) = 120 m, and East-West (EW) = 110 m	120 m
Ground control points (GCPs)	9	NA

Two single grid mission with slightly different flight height and 80% of overlap were parameterised to optimise camera calibration for multispectral imagery. An issue of uncalibrated images was observed when processing RGB images acquired using the same parameters as multispectral imagery. Therefore, the flight height, overlap, and angle of the camera were adjusted to enhance camera optimisation and generate the desired outputs. The maximum flight height of 120 m was set to acquire ground sampling distance (GSD) ≤ 15 cm in both the case. UgCS and Pix4D Crl+DJI app were used for real-time monitoring of the drone (e.g. battery and position).

2.4.2. Sampling design and plot size

A total of 35 sample plots were surveyed in the field based on a simple random sampling method. Simple random sampling is preferred over a small area with a relatively homogenous population. Since every sample has an equal chance of being selected, it has the main advantage of minimum operator bias (Hirata et al., 2012). The circular plot with an area of 500 m² (0.05 ha) was considered as a plot size for the study. The plot size was determined by considering a radius of 12.62 meters from the plot centre (*Figure 4*). Circular plots are often used as they have a small periphery and fewer trees at the borderline as compared to other plot types (Köhl et al., 2006; Maniatis & Mollicone, 2010).

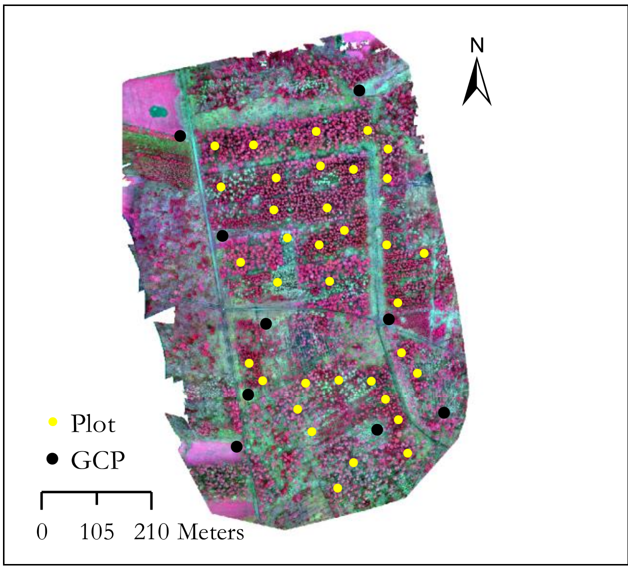

a) Spatial distribution of sample plot and GCP in the study area.

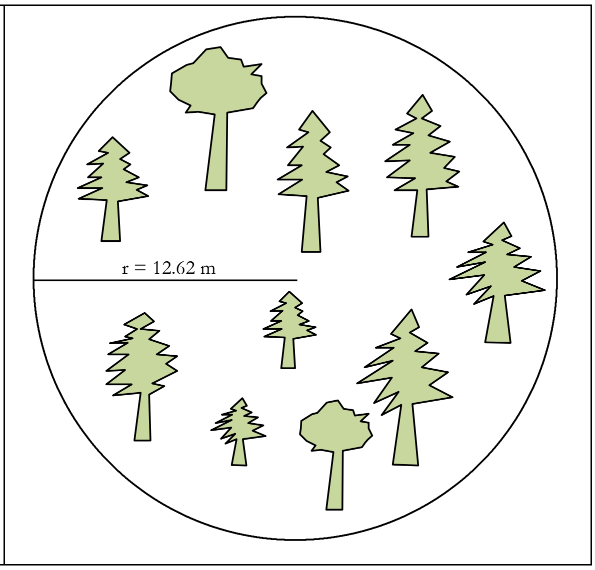

b) Schematic representation of a circular plot with 12.62 m radius.

Figure 4. Sample plot and sample plot size.

2.5. Data collection

The field data were collected between March 6 – 30, 2020. Data collection includes both UAV image acquisition and ground-truth data collection.

2.5.1. UAV image acquisition

Multispectral UAV imagery was obtained on March 6 (10:15 – 13:30 hours) using a DJI Phantom 4 quadcopter with on-board Parrot Sequoia multispectral sensor (*Figure 5b*) while UAV RGB imagery was acquired on March 30 (12:30 – 14:30 hours), 2020 using DJI Phantom 4 quadcopter RGB camera. The flight planning parameters in *Table 4* was used to acquire UAV MS and RGB imagery. The irradiance panels (AIRINOV target) was used for radiometric calibration of the multispectral sensor before the mission (*Figure 5c*). A total of nine known coordinates were placed representatively over the area using the GCP marker prior to the acquisition of UAV MS images (*Figure 4a*). All GCPs were placed in an open area, and their coordinates were measured using GNSS RTK with centimetre accuracy (*Figure 5d*).

a) Flight plan.

b) Phantom 4 quadcopter attached with Sequoia multispectral sensor.

c) Calibration target used to calibrate the MS sensor.

d) GCP marker and measurement of GCP using GNSS RTK.

Figure 5. Planning, preparation, and collection of UAV data and GCPs in the field.

2.5.2. Ground-truth data collection

Ground-truth data collection includes the measurement of individual tree parameter within the plot. Online Google Earth mobile app was used to locate the plot in the study area. The coordinates (x, y) of the plot centres were recorded using GNSS RTK. All trees in the plot were marked with a series of A4 size printed tree tag in a clockwise direction from the magnetic north (*Figure 6b*). Trees at the borderline were considered only if half (50%) of their main trunk falls within the plot perimeter. The distance (meters) and azimuth (degrees) (Grznárová et al., 2019; Lisein et al., 2013) to each tree from the plot centre were measured using distometer (Leica DISTO D510, 200 m range, ±1 mm) and Suunto compass, respectively. The species of each tree was recorded in the data collection sheet (*Appendix 7*). The girth of each tree (diameter ≥ 10 cm) was measured at 1.3 m height from the ground using a diameter tape. The height of the tree was measured using Leica DISTO D510.

a) GNSS RTK used to measure the plot centre.

b) Trees marked with tree tags to measure the distance, bearing, diameter and height.

Figure 6. A glimpse of fieldwork.

2.6. Data processing

Data processing include the processing of both ground-truth data and UAV MS and RGB images. They are presented in the following sections.

2.6.1. Ground-truth data processing

The data recorded manually in the data collection sheet was entered in Microsoft Excel. Microsoft Excel, SPSS and R (RStudio) were used to process and analyse the data. The field-based data were used to derive parameters such as the location (x, y) of an individual tree within the plot, DBH (cm tree^{-1}), tree height (m tree^{-1}), and AGB (kg tree^{-1}). The position of each tree in the plot was computed from a distance and bearing approach (Grznárová et al., 2019; Lisein et al., 2013) using the plot centre coordinate as a reference point. The calculated coordinates were imported to ArcMap to identify the trees surveyed in the field for crown delineation and tree height extraction. The same unique ID was used to match the trees surveyed in the field and their corresponding pair on the image. Descriptive statistics were used to provide summaries of sample measurements, while an allometric equation to estimate AGB/AGC.

2.6.2. UAV image processing

The photogrammetry software known as Pix4Dmapper was used to process images captured using Sequoia multispectral sensor and RGB camera. Pix4Dmapper software uses the SfM technique to generate 3D dense point cloud, DSM, DTM, and orthomosaic (Pix4D, 2017). SfM is a process to generate 3D point clouds by analysing a sequence of overlapping 2D images. It works by identifying keypoints in all images and matching the common keypoints in two or more images of the same feature (Mlambo et al., 2017; Westoby et al., 2012). Generally, there are three steps for processing images in Pix4Dmapper; i) initial processing, ii) Point cloud and mesh, iii) DSM, orthomosaic and index.

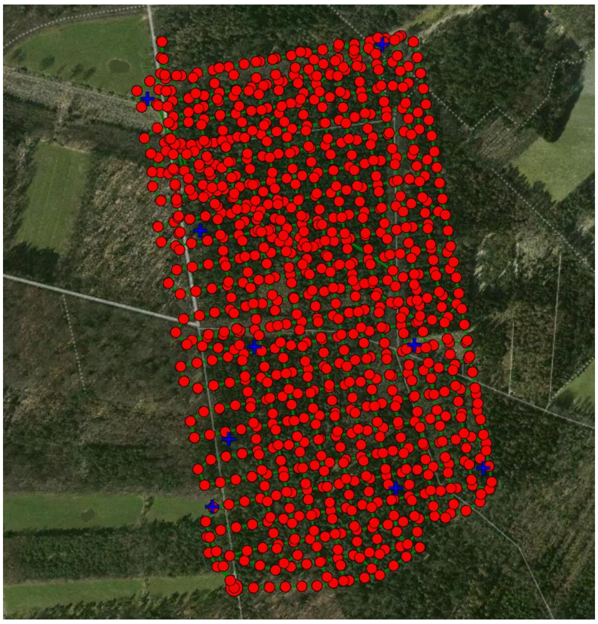

a) GCP and CP used to process the UAV images using Pix4Dmapper.

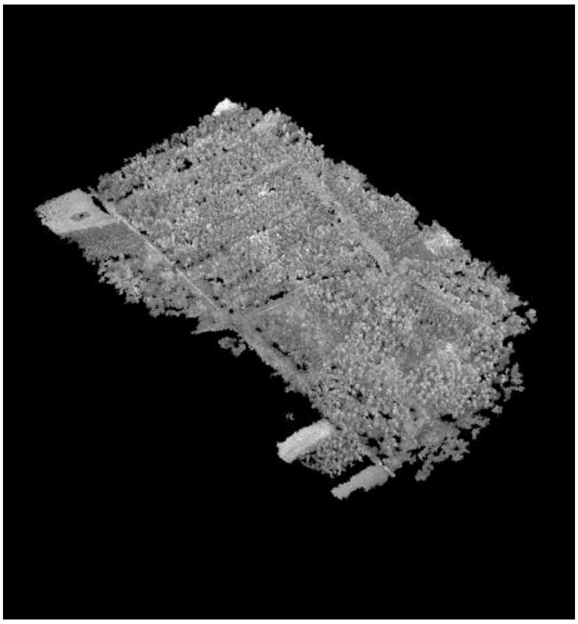

b) 3D dense point cloud generated from UAV MS images.

Figure 7. GCPs used for geolocation accuracy, and 3D dense point cloud generation.

In the first step, software extract keypoints from the images, match the same keypoints from images, calibrate internal and external camera parameters, and position the images if GCP is provided (*Figure 7*). In the second step, the software densifies the point cloud by creating extra tie points, classify the point cloud, and create 3D texture mesh using densified point cloud. In the last step, the software generates DSM, orthomosaic, DTM, reflectance and index map such as NDVI (Pix4D, 2017). The review of the principles, practices, and application of SfM in forestry can be found in Iglhaut et al. (2019).

For UAV MS images, nine known points (6 GCPs and 2 CPs) measured in the field using GNSS RTK were used to enhance geolocation accuracy, and assess the quality of the result. Regarding the UAV RGB images, eight unique features identified from MS orthomosaic were used as known points (6 GCPs and 2 CPs). The coordinate (*x, y*) were extracted from UAV MS orthomosaic, while elevation (*z*) was extracted from LiDAR-derived DTM obtained from Actueel Hoogtebestand Nederland (AHN3), respectively.

2.6.2.1. DSM, DTM and orthomosaic generation

DSM, DTM, and orthomosaic were generated automatically by the Pix4Dmapper software after densification of the point cloud. DSM represents the surface of the terrain, including both physical and human-made objects such as tree and building. Inverse Distance Weighting method was used to generate the raster DSM in Pix4Dmapper. On the contrary, the Digital Terrain Model (DTM) represent the terrain surface (Hirt, 2014). Classification of the point cloud is recommended in Pix4Dmapper to generate accurate DTM. By using the classified point cloud, the terrain is masked to create the raster DTM. The schematic illustration of DSM and DTM are presented in *Figure 8*.

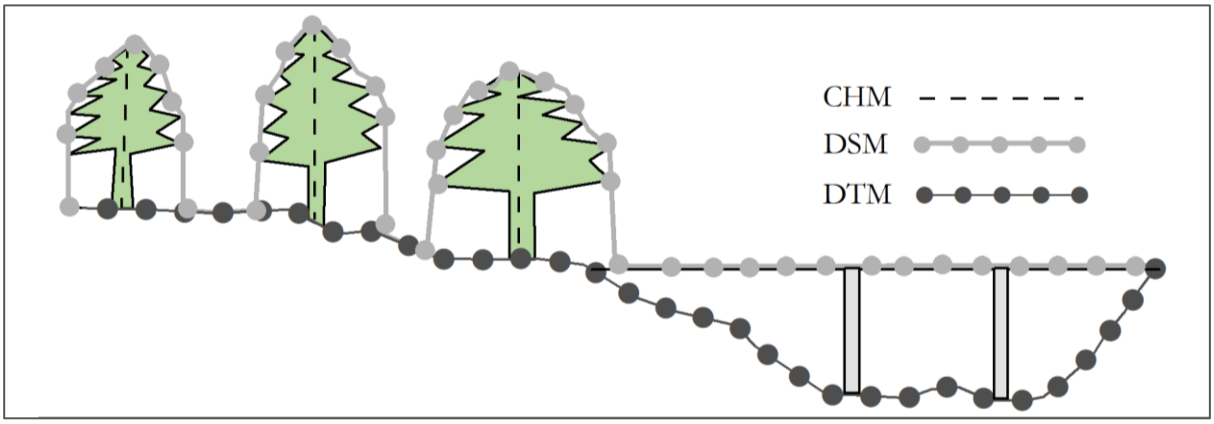

Figure 8. Schematic representation of, DSM, DTM and CHM.

The orthomosaic, also known as true orthophoto is generated using a DSM based on orthorectification. The accuracy of orthomosaic depends on the quality of DSM produced from the densified point cloud. As Pix4D generate orthomosaic of the individual band (green, red, red edge, near-infrared) for multispectral images, ERDAS IMAGINE software was used to composite these bands into a single orthomosaic.

2.6.3. LiDAR data processing

LiDAR data was obtained from Actueel Hoogtebestand Nederland (AHN) (https://www.ahn.nl/). Among various AHN products, AHN3 LiDAR data of the study area was measured in February 2019. According to AHN quality description, AHN3 measured point cloud has a height accuracy of not more than five centimetres of standard and systematic deviation, and at least 99.7% of the points have a height accuracy of 20 cm. Map Sheet *29cz1* that covers the study area was selected to download the LiDAR-derived raster DSM and DTM with a spatial resolution of 0.5 × 0.5 m. Raster calculator tool in ArcMap was used to produce CHM to extract the reference tree height.

2.7. Data analysis

Data analysis includes the accuracy assessment of forest parameters, model development to predict DBH and model validation. They are presented in the following sections.

2.7.1. Crown delineation

Multispectral and RGB orthomosaic were used to delineate each tree crowns surveyed in the field using manual on-screen digitisation (*Figure 9*). Manual on-screen digitising is preferred at a plot level as it is more accurate (Pouliot et al., 2002) and requires no accuracy assessment. The map scale at 1:50 was used while digitising the tree crowns to obtain the same detail of crown structure irrespective of the size. Those trees not identified on the orthomosaic due to the understory occlusion were noted to exclude for comparison and accuracy assessment.

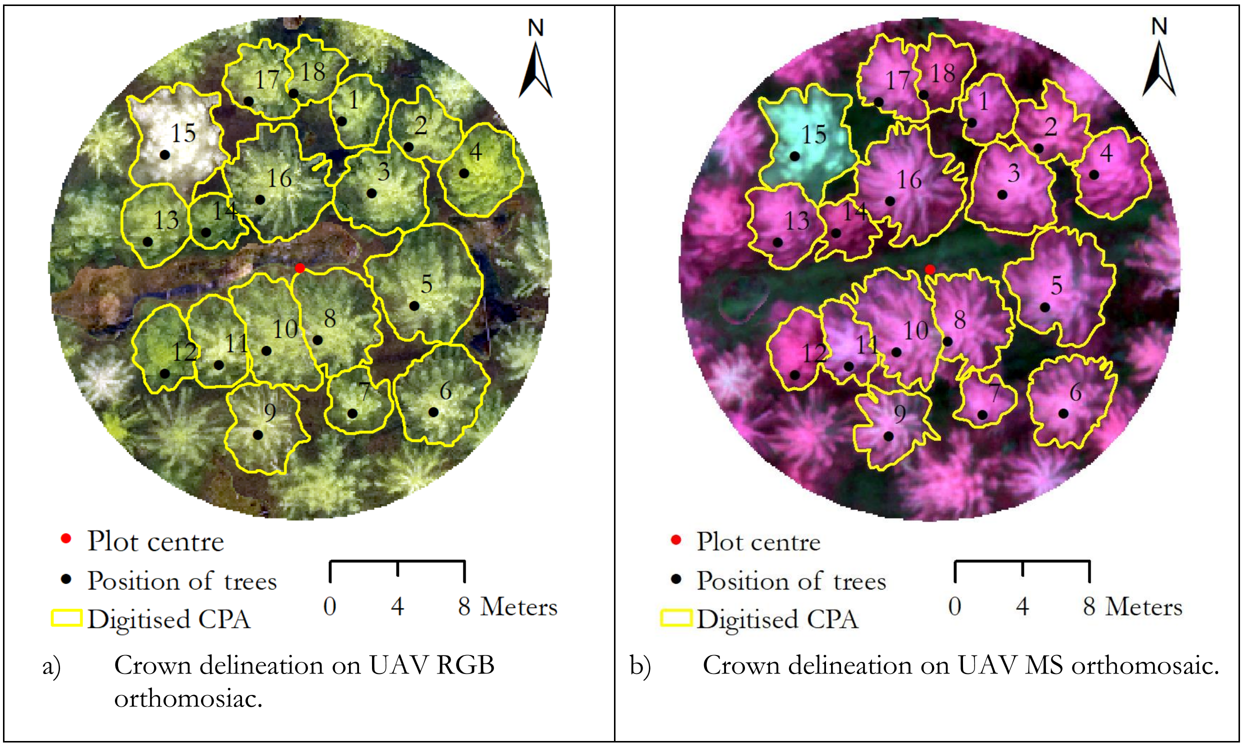

Figure 9. CPA delineation using manual on-screen digitisation.

2.7.2. Generation of crown diameter

Manually digitised tree crown from UAV MS, and RGB orthomosaic was used to derive tree crown diameter using *Eq.* (1). The *t*-test was used to test the significant difference of mean crown diameter derived from UAV MS and RGB orthomosaic at $\alpha = 0.05$.

$$\mathrm{CD} = \sqrt{\frac{\mathrm{CPA}}{\pi}} \tag{1}$$

Where:
CD = crown diameter (m)
CPA = canopy projection area (m^2)
$\pi = \sim 3.14159$.

2.7.3. CHM generation

CHM represents the height of the trees between treetop and the ground (*Figure 8*). Raster calculator tool in ArcMap was used to compute CHM by subtracting raster DTM from raster DSM.

2.7.4. Tree height extraction

The CHM is often used to extract tree height information (Iizuka et al., 2017). The maximum value of CHM within the CPA was considered as the tree height. The MS and RGB-derived CPA was overlayed on the respective UAV CHM to extract tree height using zonal statistics tool in ArcMap. MS-derived CPA was used to extract the LiDAR tree height from LiDAR CHM, assuming it as a more accurate delineation of the tree crown.

2.7.5. Tree height accuracy

The common method to assess the accuracy is to pair the remote sensing estimated parameter with a reference parameter to quantify their consistency using statistical analysis. Linear regression was established between tree height estimated from UAV CHM and reference tree height from LiDAR. The Pearson's correlation coefficient (r) and coefficient of determination (R^2) were used to assess the accuracy of UAV-estimated tree height, while Root Mean Square Error (RMSE) and bias were used to quantify the deviation of UAV-estimated tree height from the LiDAR-measured tree height as proposed by Yin and Wang (2016). The accuracy metrics are presented in *Eq.* (2) - (7) (Yin & Wang, 2016). One-way ANOVA *F*-test was used to test the significant difference ($\alpha = 0.05$) among the group means of tree height. Follow-up test (Tukey post hoc) was used when the null hypothesis was rejected to test the significant difference between each group means of tree height.

$$r = \frac{\sum \left((x_{est} - \overline{x_{est}}) (x_{obs} - \overline{x_{obs}}) \right)}{\sqrt{\sum (x_{est} - \overline{x_{est}})^2 \sum (x_{obs} - \overline{x_{obs}})^2}} \quad (2)$$

$$R^2 = r^2 \quad (3)$$

$$RMSE = \sqrt{\frac{\sum (x_{est} - x_{obs})^2}{(n_{pair} - 1)}} \quad (4)$$

$$RMSE\ (\%) = \frac{RMSE}{\overline{x_{obs}}} \times 100 \quad (5)$$

$$bias = \frac{\sum (x_{est} - x_{obs})}{(n_{pair} - 1)} \quad (6)$$

$$bias\ (\%) = \frac{bias}{\overline{x_{obs}}} \times 100 \quad (7)$$

Where:

x_{est} is the estimated values

x_{obs} is the observed (reference values)

n_{pair} is the number of paired samples

$\overline{x_{est}}$ and $\overline{x_{obs}}$ are average values of x_{est} and x_{obs}, respectively.

2.7.6. Model development to predict DBH

Different regression models were developed to predict tree DBH using parameters derived from UAV imagery. In all the models, DBH was used as a function of either *TH, CPA, CD* or the combination of *TH* and *CD* as a compound variable (*TH* × *CD*). *TH* × *CD* was used as a compound variable rather than two predictors independently to avoid the issue of collinearity (Dormann et al., 2013; Jucker et al., 2017). The dataset was randomly split into 60% and 40% for model development and model validation, respectively. The 60% (380 trees) of the DBH and its corresponding crown diameter and tree height derived from UAV imagery was used to establish the relationship.

2.7.7. DBH prediction and validation

The equation of the non-linear quadratic function from model development was used to predict the DBH. Linear regression was established between ground-truth DBH and predicted DBH to validate the predicted DBH using 40% (250 trees) of validation dataset. The r and R^2 were used to assess the accuracy of the predicted DBH. Other metrics such as RMSE and bias was used to quantify the deviation of the predicted DBH from the reference DBH. The difference in observed and predicted value was treated as errors. The residuals were plotted on the graph against the reference DBH to provide an overview of model performance (Chai & Draxler, 2014).

2.7.8. Assessment of AGB

The typical non-destructive way to estimate forest biomass and continuous growth is using an allometric equation. Several allometric equations have been developed over the years based on the destructive harvest method. The non-destructive way is crucial to assess the temporal variation in forest biomass through a time-series of measurement. Since allometric equations are species-specific, *Eq.* (8) - (11) were used to estimate AGB of four conifer species (*Table 5*). One-way ANOVA *F*-test was used to test the significant difference ($\alpha = 0.05$) among the group means of estimated AGB.

Table 5. The species-specific allometric equation used to estimate AGB.

Species	Allometric equation	n	R^2	Reference	Eq.
Norway spruce	$AGB = a\,D^b\,H^c$ Where; a = 0.054 b = 1.847 c = 0.826	254	0.98	Fehrmann and Kleinn (2006)	(8)
Scots pine	$AGB = a\,D^b\,H^c$ Where; a = 0.03191 b = 1.89823 c = 0.89868	52	0.99	Cienciala et al. (2006)	(9)
Douglas-fir	$\ln(AGB) = a + b\ln(D)$ Where; a = - 1.620 b = 2.410	23	0.99	Bartelink (1996)	(10)
Larix decidua	$AGB = a\,D^b\,H^c$ Where; a = 0.0188 b = 1.9093 c = 1.0805	96	0.98	Jagodziński et al. (2018)	(11)

Where:
AGB is the aboveground biomass (kg $tree^{-1}$)
D is the DBH (cm $tree^{-1}$)
H is the tree height (m $tree^{-1}$).

2.7.9. Assessment of AGC

In general, carbon accounts for half of the biomass. Therefore, 0.5 (Hirata et al., 2012) was used as a carbon conversion factor to estimate the AGC using *Eq.* (12). The conversion factor is a fraction of biomass that is carbon.

$$C = AGB \times CF \tag{12}$$

Where;
C = carbon (kg)
CF = conversion factor

2.7.10. Accuracy assessment of AGB/AGC

The reference AGB/AGC assessed from the field with LiDAR, and AGB/AGC estimated from UAV imagery were plotted on vertical (*y*) and horizontal (*x*) axis respectively to establish the linear regression. Through linear regression, the accuracy of the estimated AGB/AGC was assessed using a statistical indicator such as r and R^2. Moreover, RMSE and bias were used to quantify the magnitude of deviation of the estimated AGB/AGC from the reference AGB/AGC. The accuracy metrics are presented in *Eq.* (2) - (7). Simple *t*-test was used to test the significant relationship between a field with LiDAR-based and UAV-based AGB using *Eq.* (13).

$$t = \frac{b_1 - 0}{s} = \frac{b_1}{\left(\sqrt{\frac{MS_{residual}}{\sum (x_i - \bar{x})^2}}\right)} \tag{13}$$

Where:
b_1 = regression coefficient
s = standard error of the regression

3. RESULT

3.1. Groud-truth result

This section includes the result of tree parameters measured in the field. DBH and tree height of 650 trees in 35 plots were measured in the study area. On average, 19 trees were observed in each plot with a minimum and maximum of 8 and 36 trees, respectively (*Figure 10*).

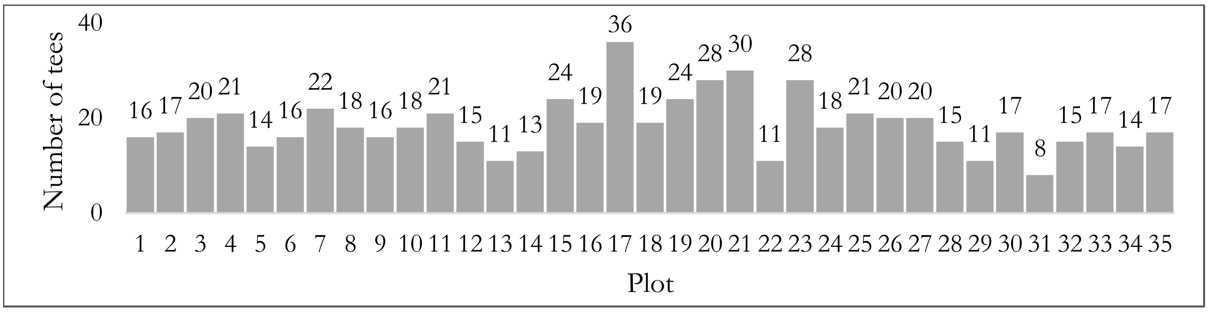

Figure 10. Plot-wise distribution of trees.

Norway spruce constituted a maximum sample with 425 trees followed by Scots pine with 83 trees. Douglas-fir and European larch comprised of 72 and 70 trees, respectively (*Table 6*). The distribution of species in each plot is presented in *Appendix 2*.

Table 6. Descriptive statistics of field-measured DBH by species.

Parameter	Species	n	Minimum	Maximum	Mean	Std. Deviation
DBH (cm)	Norway spruce	425	11	52	28.10	8.52
	Scots pine	83	12	59	39.46	10.60
	Douglas-fir	72	12	61	35.31	12.60
	Larch	70	12	44	24.49	7.78

3.1.1. Diameter at breast height

Mean tree DBH measured in the field was 29.96 cm with the minimum and maximum of 11 and 61 cm, respectively. The standard deviation of the DBH was 10.27 cm. Among the species, the highest and lowest mean DBH was found in Scots pine and European larch, respectively (*Table 6*). The histogram and normal Q-Q plot of field-measured tree DBH are presented in *Figure 11*.

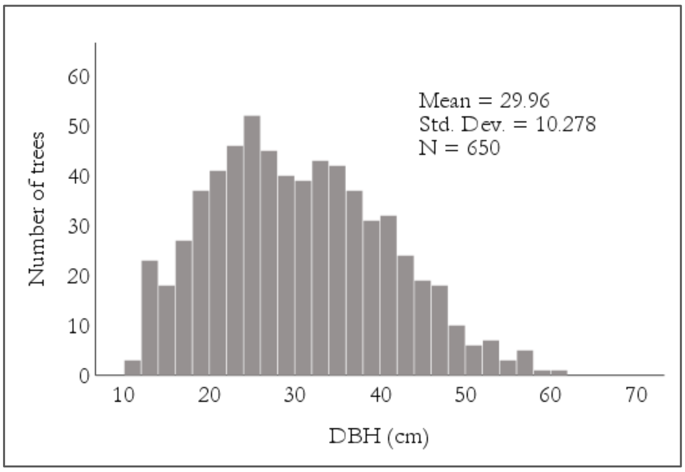

a) Histogram.

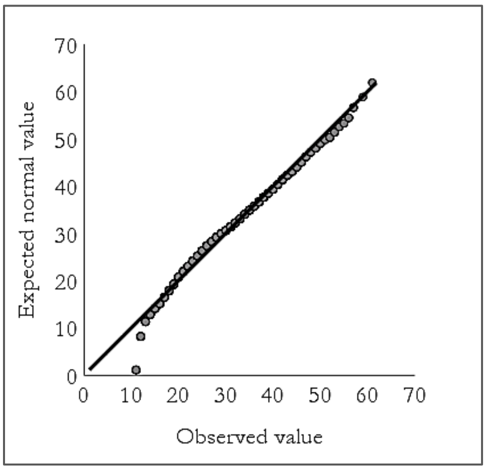

b) Normal Q-Q plot.

Figure 11. Histogram and normal Q-Q plot of field-measured tree DBH.

3.2. Field-measured tree height

Mean tree height measured in the field was 21.26 m ranging between 6 to 35 m (*Appendix 1*). The standard deviation of the tree height was 4.59 m. The histogram and normal Q-Q plot of field-measured tree height are shown in *Figure 12*.

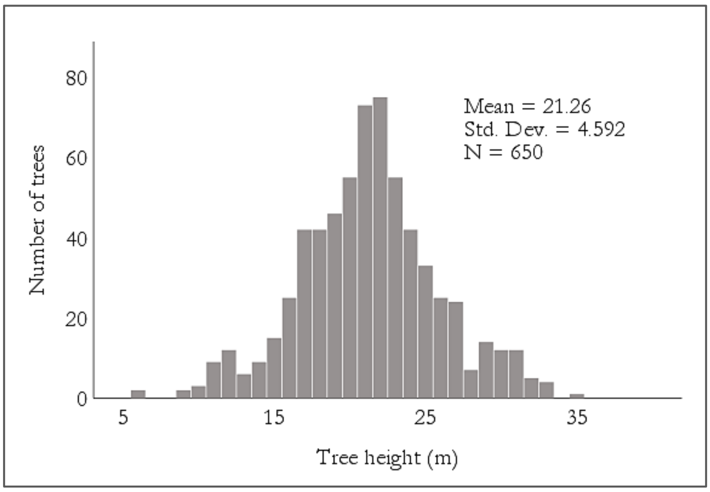

a) Histogram.

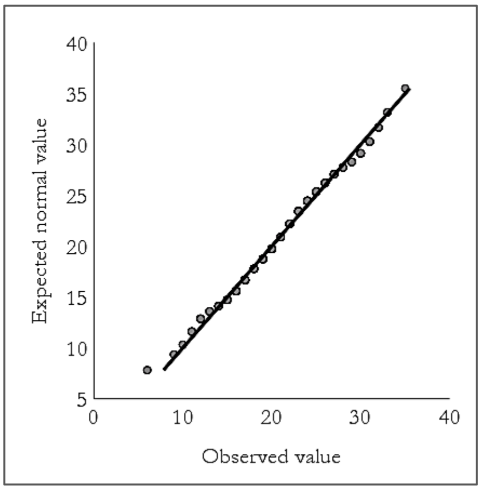

b) Normal Q-Q plot.

Figure 12. Histogram and normal Q-Q plot of field-measured tree height.

3.3. UAV-based result

This section includes the result of processed UAV images such as orthomosaic, DSM, DTM, and CHM. Overview of results from processed UAV MS and RGB imagery is presented in *Appendix 3*.

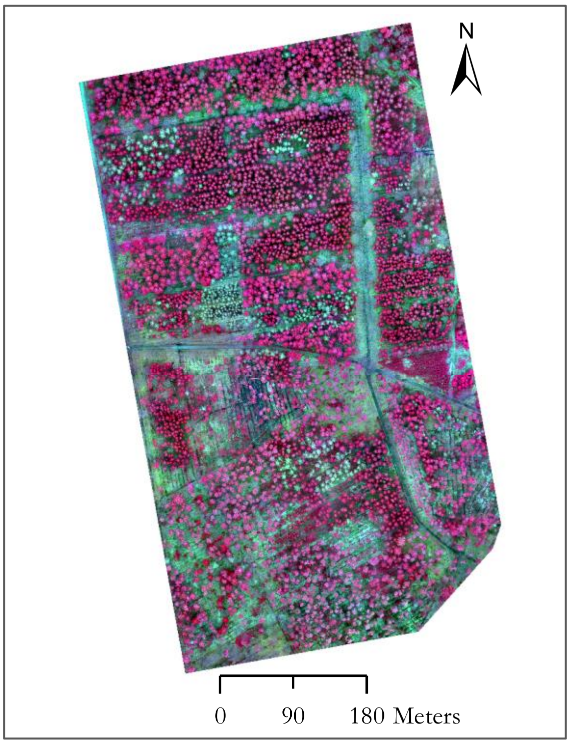

a) Multispectral orthomosaic.

b) RGB orthomosaic.

Figure 13. Orthomosaic of UAV MS and RGB images of the study area.

3.3.1. Orthomosaic

The Amersfoort (RD New) coordinate system was used for all the spatial dataset. The spatial resolution of multispectral orthomosaic was 0.10 × 0.10 m (*Figure 13a*). The spatial resolution of RGB orthomosaic was resampled to 0.10 × 0.10 m (*Figure 13b*) from 0.04 × 0.04 m.

3.3.2. DSM, DTM and CHM

The spatial resolution of multispectral DSM and DTM was 0.10 × 0.10 m and 0.53 × 0.53 m, respectively. The cell size of MS CHM was generated the same as MS DSM (*Figure 14*). The mean height of the study area from MS DSM and DTM was 62 and 50 m, respectively.

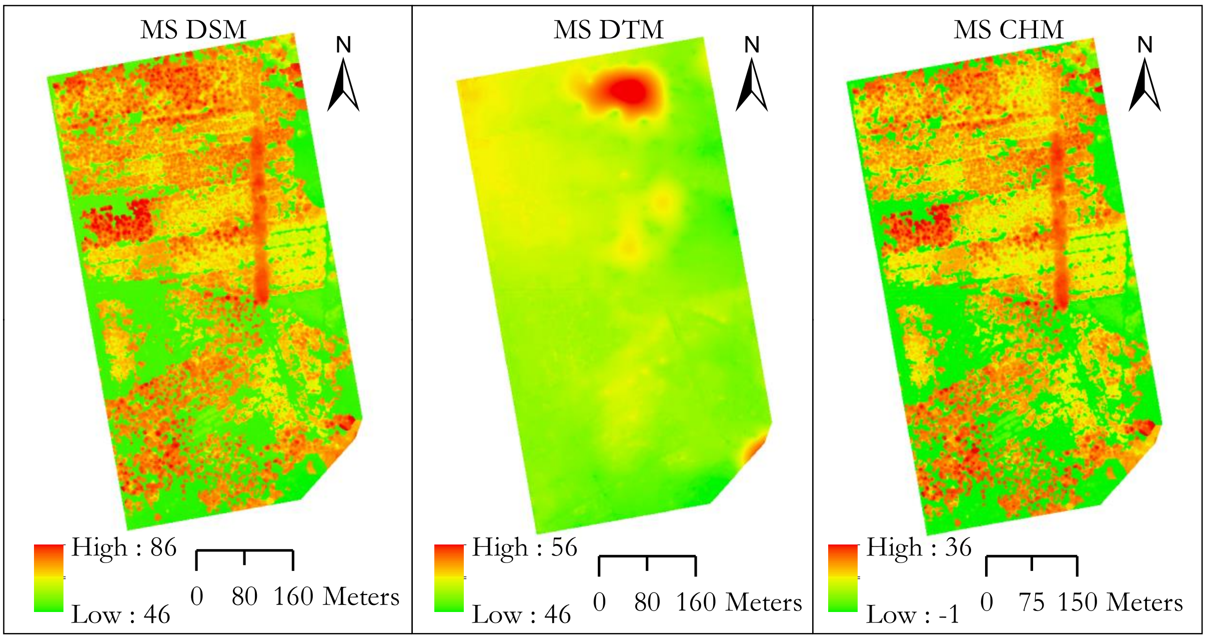

Figure 14. Multispectral DSM, DTM, and CHM.

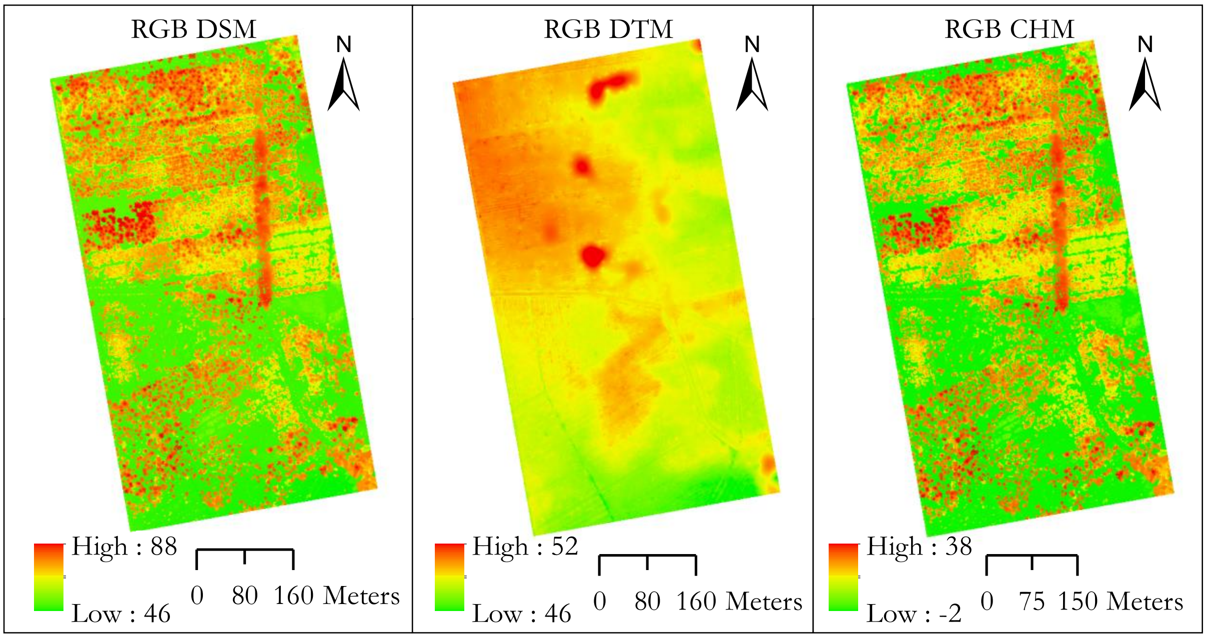

Figure 15. RGB DSM, DTM, and CHM.

The spatial resolution of RGB DSM and DTM was 0.04 × 0.04 m and 0.23 × 0.23 m, respectively. The cell size of RGB CHM was generated the same as RGB DSM and resampled to 0.10 × 0.10 m (*Figure 15*). The mean height of the study area from RGB DSM and DTM was 60 and 49 m, respectively.

The mean height of the study area from CHM was higher for UAV MS imagery (12 m) as compared to UAV RGB imagery (11 m). However, the maximum frequency of tree height in MS and RGB was observed in 18, and 19 m, respectively (*Figure 16*).

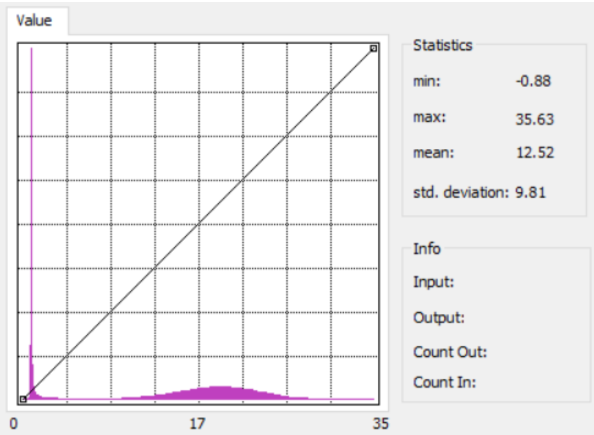

a) Histogram of MS CHM.

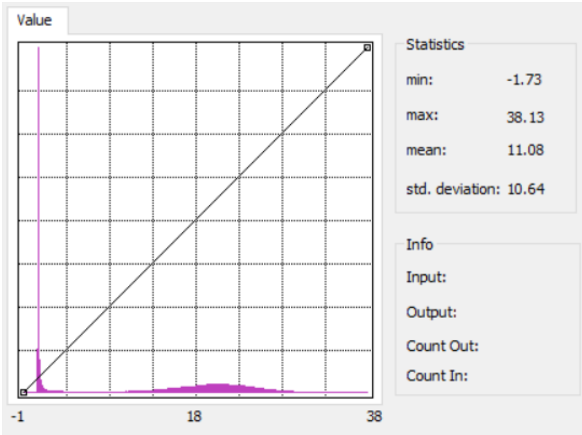

b) Histogram of RGB CHM.

Figure 16. Histogram of UAV MS and RGB CHM.

3.4. Canopy projection area

The crowns of 630 trees were manually digitised from UAV MS and RGB orthomosaic. However, 20 trees were not identified on orthomosaic due to occlusion from the tall trees. The average height of the occluded trees was 12 m.

The mean CPA digitised from the multispectral orthomosaic was 17.79 m² with the smallest and largest crown size of 0.41 and 80.65 m², respectively. The standard deviation of the MS CPA was 12.18 m². Likewise, mean CPA from RGB orthomosaic was 18.51 m² ranging from 0.62 to 78.04 m². The standard deviation of RGB CPA was 12.51 m². The histogram of MS and RGB CPA is shown in *Figure 17*.

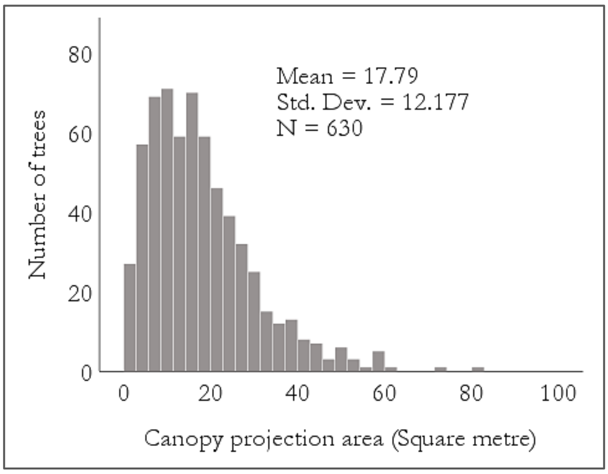

a) Histogram of CPA derived from UAV MS imagery.

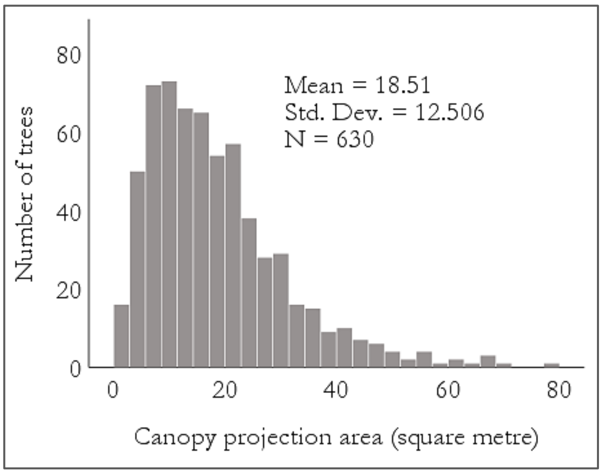

b) Histogram of CPA derived from UAV RGB imagery.

Figure 17. Histogram of CPA digitised from MS and RGB orthomosaic.

3.5. Crown diameter

The mean crown diameter derived from CPA of MS orthomosaic was 2.24 m with the smallest and largest crown diameter of 0.36 and 5.07 m, respectively. The standard deviation of the MS crown diameter was 0.80 m. The mean crown diameter derived from CPA of RGB orthomosaic was 2.29 m ranging between 0.44 to 4.98 m. The standard deviation of RGB crown diameter was 0.79 m. The histogram and descriptive statistics are presented in *Figure 18* and *Table 7*, respectively.

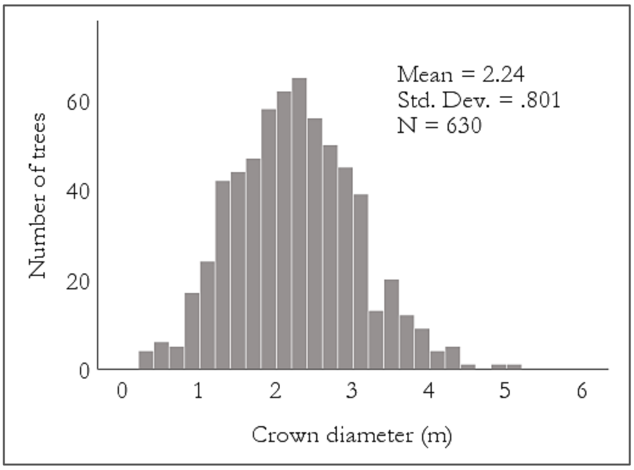

a) Histogram of crown diameter derived from UAV MS imagery.

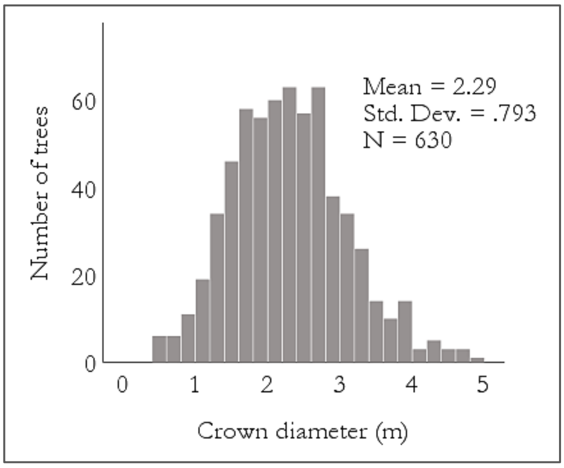

b) Histogram of crown diameter derived from UAV RGB imagery.

Figure 18. Histogram of the crown diameter obtained from MS and RGB CPA.

Table 7. Descriptive statistics of crown diameter derived from UAV MS and RGB CPA.

	N	Minimum	Maximum	Mean	Std. Deviation
MS crown diameter (m)	630	0.36	5.07	2.24	0.80
RGB crown diameter (m)	630	0.44	4.98	2.29	0.79

3.5.1. Comparison of crown diameter

A strong positive correlation ($R^2 = 0.96$) was found between crown diameter derived from UAV MS and RGB orthomosaic. The standard error of crown diameter estimate was 0.16 m. The scatter plot and regression statistics are presented in *Figure 19* and *Table 8*, respectively.

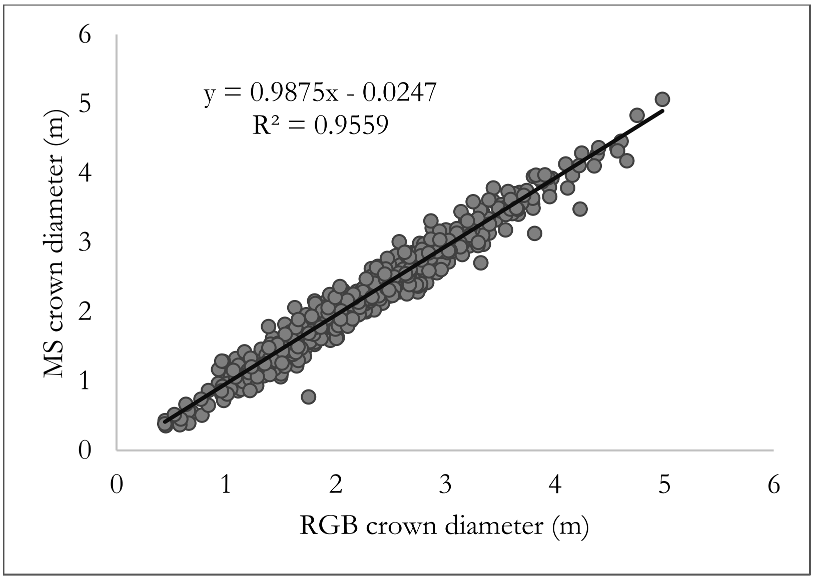

Figure 19. Scatter plot of CPA-derived MS and RGB crown diameter.

Among the species, the highest correlation between MS and RGB-derived crown diameter was found in Douglas-fir (R^2 = 0.96), and Larix decidua (R^2 = 0.96) followed by Norway spruce (R^2 = 0.95) and Scots pine (R^2 = 0.93).

Table 8. Regression statistics of UAV MS and RGB crown diameter.

r	R Square	Adjusted R Square	Std. Error of the Estimate
0.98	0.96	0.96	0.17

3.5.2. Crown diameter hypothesis testing

T-test (assuming equal variances) showed no significant difference of mean tree crown diameter (t = -1.19, df = 1258, p > 0.05) derived from UAV MS and RGB imagery. The test result is shown in *Table 9*.

Table 9. T-Test: Two-Sample Assuming Equal Variances of crown diameter.

	MS CD (m)	RGB CD (m)
Mean	2.24	2.29
Variance	0.64	0.63
Observations	630	630
Pooled Variance	0.64	
Hypothesized Mean Difference	0.00	
df	1258	
t Stat	-1.19	
P(T<=t) one-tail	0.12	
t Critical one-tail	1.65	
P(T<=t) two-tail	0.24	
t Critical two-tail	1.96	

3.6. UAV tree height

The mean tree height extracted from UAV MS CHM was 20.33 m ranging between 10.81 and 30.82 m. The standard deviation of the MS tree height was 3.48 m. Similarly, the mean tree height extracted from of UAV RGB CHM was 22.19 m with minimum and maximum tree height of 10.57 and 34.60 m, respectively. The standard deviation of RGB tree height was 3.9 m. The histogram and descriptive statistics of tree height are presented in *Figure 20* and *Table 10*, respectively.

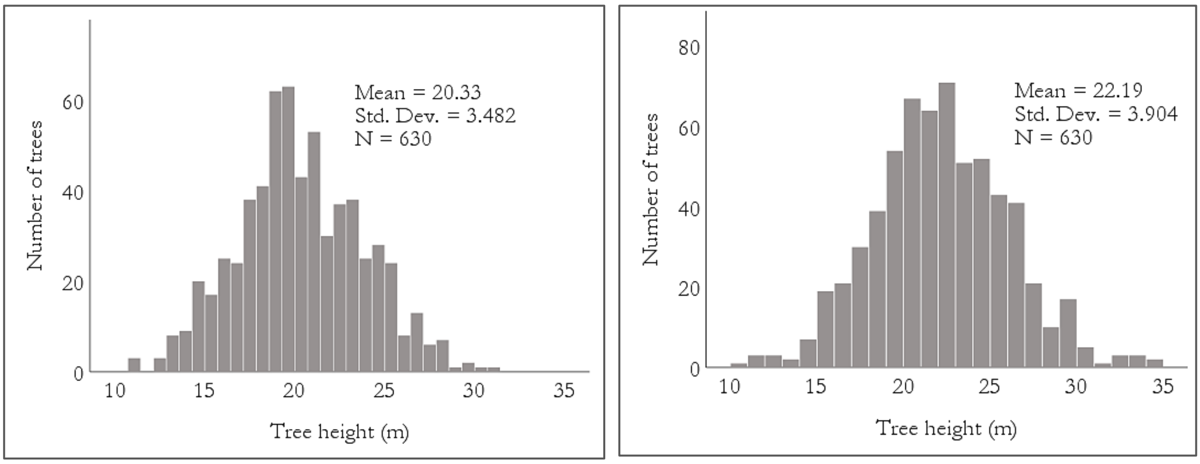

a) Histogram of MS tree height. b) Histogram of RGB tree height.

Figure 20. Histogram of tree height obtained from CHM of UAV MS and RGB imagery.

Table 10. Descriptive statistics of UAV derived tree height.

	n	Minimum	Maximum	Mean	Std. Deviation
UAV MS TH (m)	630	10.81	30.82	20.33	3.48
UAV RGB TH (m)	630	10.57	34.60	22.19	3.90

3.7. LiDAR tree height

The spatial resolution of LiDAR DSM and DTM was 0.5 × 0.5 m. The cell size of LiDAR CHM was generated the same as LiDAR DSM (*Figure 21*). Mean tree height derived from LiDAR CHM was 19.75 m, ranging from 6.07 to 30.96 m. The standard deviation of the tree height was 4.04 m. The histogram and normal Q-Q plot of LiDAR-measured tree height are shown in *Figure 22*.

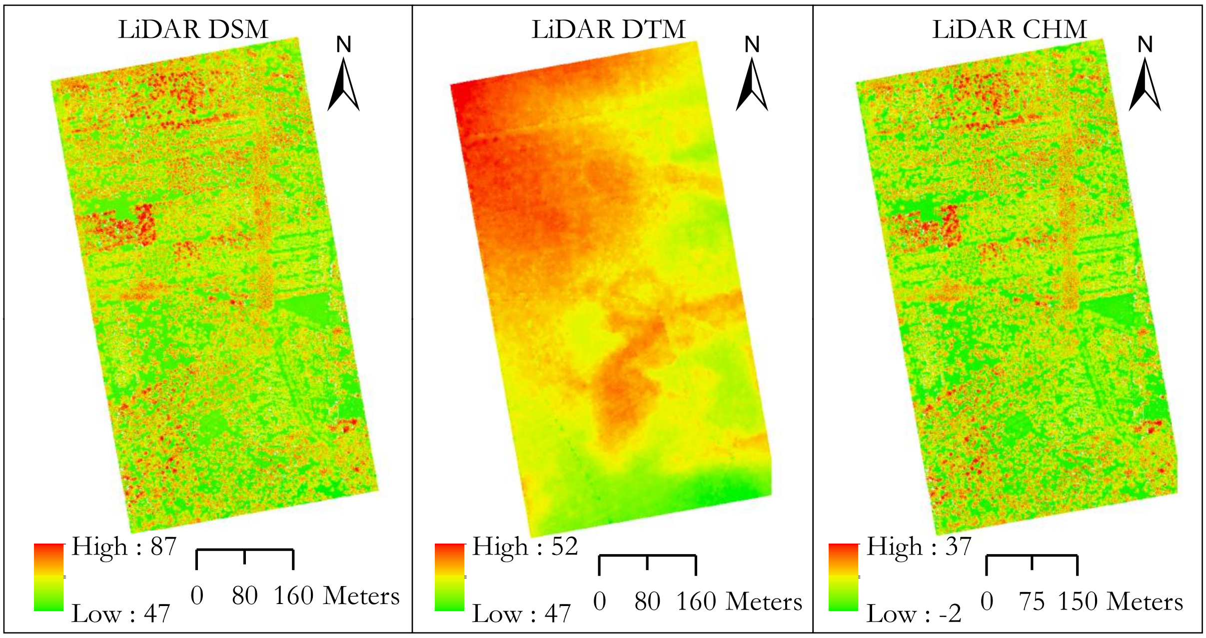

Figure 21. LiDAR DSM, DTM, and CHM.

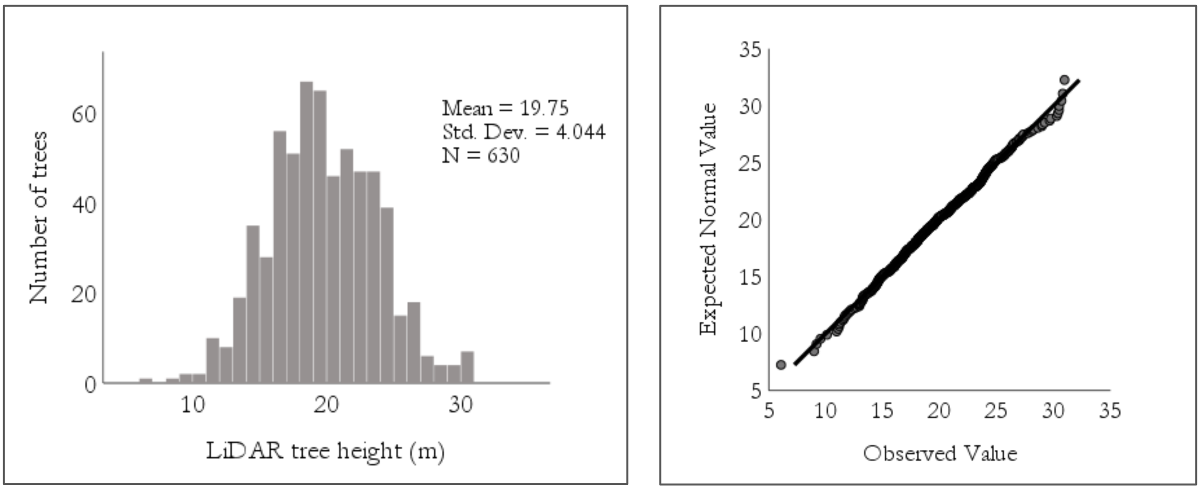

a) Histogram. b) Normal Q-Q plot.

Figure 22. Histogram and normal Q-Q plot of LiDAR-measured tree height.

3.8. Tree height accuracy

3.8.1. Field and LiDAR-measured tree height

Tree height measured in the field showed fair agreement (R^2 = 0.73; RMSE = 2.91 m) with tree height derived from LiDAR. Field-measured tree height tended to overestimate tree height (bias = 9.14%). The scatter plot and regression statistics are presented in *Figure 23* and *Table 11*, respectively.

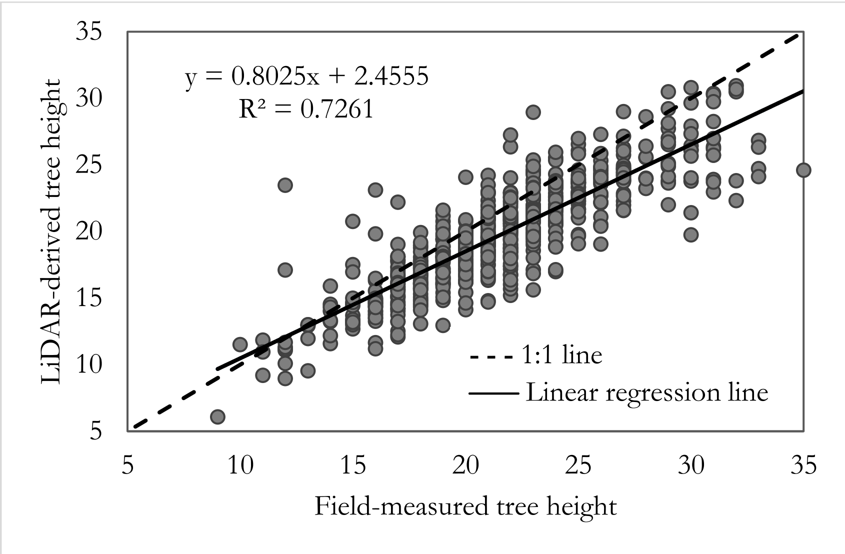

Figure 23. Scatter plot of field and LiDAR-measured tree height.

Table 11. Regression statistics of field and LiDAR-measured tree height.

r	R Square	Std. Error of the Estimate	RMSE	RMSE %	Bias	Bias %
0.85	0.73	2.12	2.91	14.72	1.81	9.14

3.8.2. UAV MS and LiDAR tree height

Tree height estimated from UAV MS CHM showed reasonable agreement (R^2 = 0.79; RMSE = 1.94 m) with tree height derived from LiDAR. MS CHM-derived tree height tended to overestimate (bias = 2.90%) tree height slightly. The scatter plot and regression statistics are presented in *Figure 24* and *Table 12*, respectively.

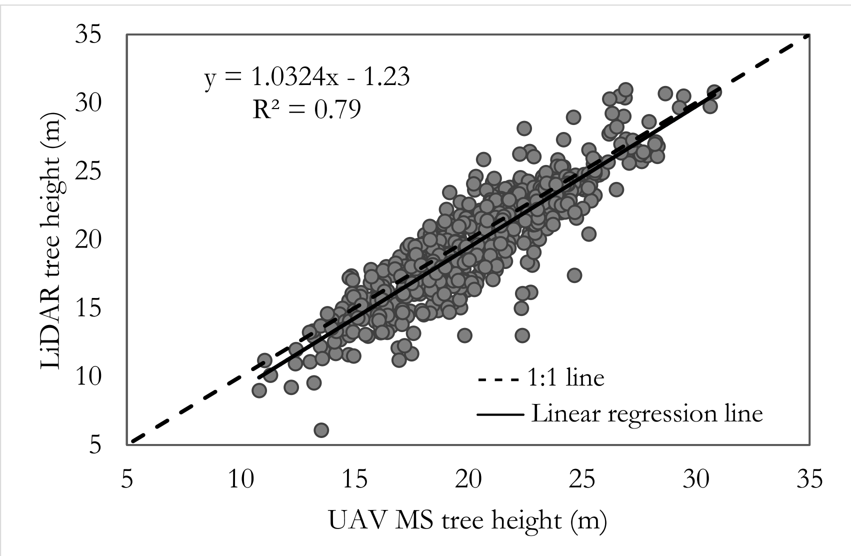

Figure 24. Scatter plot of MS CHM-derived and LiDAR-measured tree height.

Table 12. Regression statistics of UAV MS-derived and LiDAR-measured tree height.

r	R Square	Std. Error of the Estimate	RMSE	RMSE %	Bias	Bias %
0.89	0.79	1.86	1.94	9.83	0.57	2.90

3.8.3. UAV RGB and LiDAR tree height

Tree height estimated from UAV RGB CHM showed reasonable agreement ($R^2 = 0.83$; RMSE = 2.95 m) with tree height derived from LiDAR. RGB CHM-derived tree height tended to overestimate tree height (bias = 12.33%). The R^2 of RGB CHM-derived tree height was slightly higher than MS CHM-derived tree height. The scatter plot and regression statistics are shown in *Figure 25* and *Table 13*, respectively.

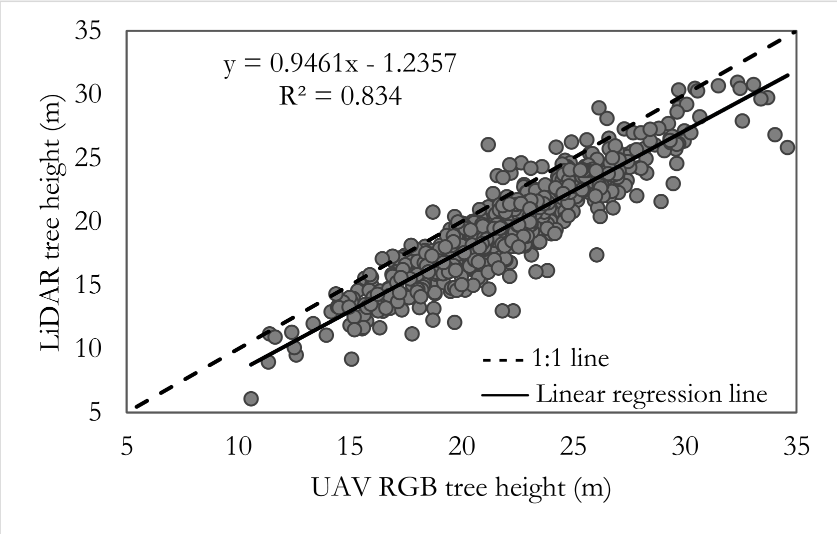

Figure 25. Scatter plot of RGB CHM-derived and LiDAR-measured tree height.

Table 13. Regression statistics of UAV RGB-derived and LiDAR-measured tree height.

r	R Square	Std. Error of the Estimate	RMSE	RMSE %	Bias	Bias %
0.91	0.83	1.65	2.95	14.92	2.44	12.33

3.8.4. Tree height hypothesis testing

One-way ANOVA *F*-test (*Table 14*) showed a significant difference of mean tree height ($F(2, 1887) = 69.90$, $p < 0.05$). The follow-up Tukey post hoc tests showed a significant difference between the mean tree height from LiDAR and MS CHM ($p < 0.05$), as well as from LiDAR and RGB CHM ($p < 0.05$). Also, a significant difference was found between the mean tree height from MS CHM and RGB CHM ($p < 0.05$). The test result is presented in *Table 1Table 15*.

Table 14. One-way ANOVA test of tree height.

SUMMARY						
Groups	**Count**	**Sum**	**Average**	**Variance**		
LiDAR TH (m)	630	12445.38	19.75	16.36		
UAV MS TH (m)	630	12805.25	20.33	12.12		
UAV RGB TH (m)	630	13977.35	22.19	15.24		
ANOVA						
Source of Variation	**SS**	**df**	**MS**	**F**	**P-value**	**F crit**
Between Groups	2037.17	2	1018.59	69.90	0	3.00
Within Groups	27498.07	1887	14.57			
Total	29535.25	1889				

Table 15. Post Hoc test (Tukey HSD) of tree height.

Multiple comparisons		Mean Difference	Std. Error	Sig.	95% Confidence Interval	
					Lower Bound	Upper Bound
LiDAR TH	MS TH	-.57*	0.22	0.02	-1.08	-0.07
	RGB TH	-2.43*	0.22	0.00	-2.94	-1.93
MS TH	LiDAR TH	.57*	0.22	0.02	0.07	1.08
	RGB TH	-1.86*	0.22	0.00	-2.36	-1.36
RGB TH	LiDAR TH	2.43*	0.22	0.00	1.93	2.94
	MS TH	1.86*	0.22	0.00	1.36	2.36

* The mean difference is significant at the 0.05 level.

3.9. Estimating tree DBH from UAV imagery

3.9.1. Multispectral model development

A total of 380 trees were used to develop the model. Among the models, tree height × crown diameter *(TH × CD)* proved a better predictor explaining 84% of observed DBH variance compared to lone predictor such as *TH, CPA, CD* (*Table 16*). The quadratic model (D_{pred} = -0.0019 (TH × CD)^2 + 0.6219 (TH × CD) + 6.3708) was used to predict tree DBH since the model performance was better than other models in terms of both R^2 and RMSE. The scatter plot and model summary is shown in *Figure 26* and *Table 17*, respectively.

Table 16. MS model development summary.

Model	Predictor (x)	Equation	R^2	RMSE	Bias (%)
Linear	TH	y = 2.2676x - 15.546	0.589	6.428	0.002
Linear	CPA	y = 0.6982x + 18.027	0.696	5.526	0.001
Linear	CD	y = 10.924x + 5.9376	0.744	5.070	0.003
Linear	TH × CD	y = 0.4034x + 11.447	0.825	4.198	-0.008
Logarithmic	TH × CD	y = 17.418ln(x) - 34.542	0.799	4.489	0.004
Power	TH × CD	$y = 2.9262x^{0.6127}$	0.843	4.016	-0.934
Quadratic	TH × CD	$y = -0.0019x^2 + 0.6219x + 6.3708$	0.847	3.918	0.085

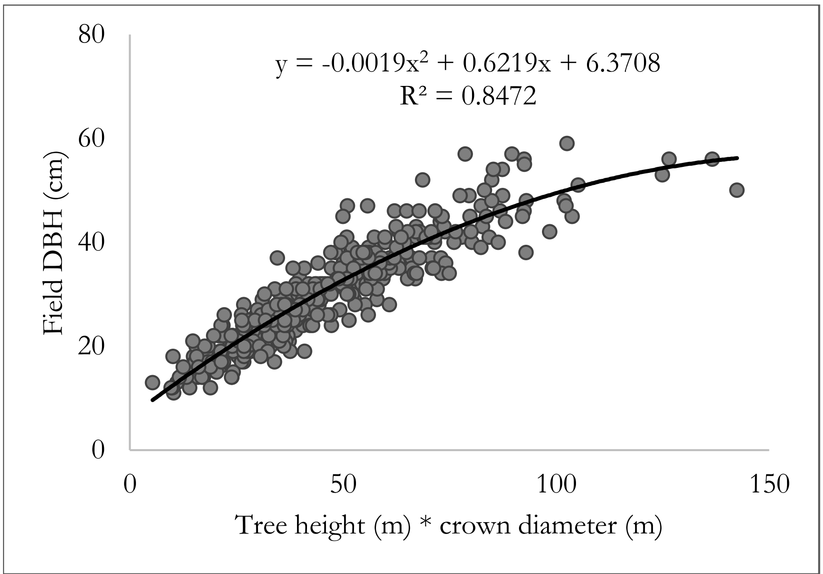

Figure 26. Relationship between field-measured DBH and UAV MS-derived TH × CD.

Table 17. Summary of MS model used to predict tree DBH.

r	R square	Std. Error of the Estimate	RMSE	RMSE %	Bias	Bias %
0.920	0.847	3.928	3.918	12.902	0.026	0.085

3.9.2. RGB model development

The power model performed slightly better by explaining 84% of observed DBH variance as compared to other models. However, the RMSE and bias of the power model were slightly higher than the quadratic model (*Table 18*). Moreover, the quadratic model performed slightly better in model validation than the power model (*Appendix 4*). Therefore, the quadratic model (D_{pred} = -0.0018 (TH × CD)^2 + 0.5871 (TH × CD) + 5.4961) was used to predict tree DBH. The scatter plot and model summary is shown in *Figure 27* and *Table 19*, respectively.

Table 18. RGB model development summary.

Model	Predictor (x)	Equation	R^2	RMSE	Bias (%)
Linear	TH	y = 2.1093x - 16.195	0.629	6.108	-0.003
Linear	CPA	y = 0.6883x + 17.732	0.695	5.535	0.002
Linear	CD	y = 11.164x + 4.8064	0.749	5.023	-0.003
Linear	TH × CD	y = 0.36x + 11.458	0.804	4.437	0.005
Logarithmic	TH × CD	y = 17.655ln(x) - 37.492	0.795	4.541	0.005
Power	TH × CD	$y = 2.5981x^{0.6249}$	0.849	4.194	-0.931
Quadratic	TH × CD	$y = -0.0018x^2 + 0.5871x + 5.4961$	0.834	4.082	-0.384

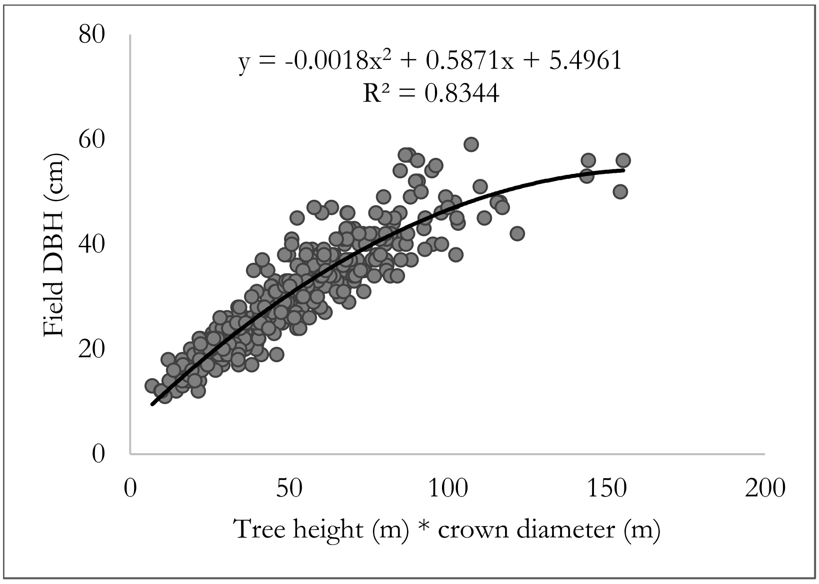

Figure 27. Relationship between field-measured DBH and UAV RGB-derived TH × CD.

Table 19. Summary of the RGB model used to predict tree DBH.

r	R Square	Std. Error of the Estimate	RMSE	RMSE %	Bias	Bias %
0.913	0.834	4.089	4.082	13.441	-0.117	-0.384

3.9.3. Multispectral model validation

A total of 250 trees was used to validate the model. A strong positive correlation (r = 0.91) was observed between DBH predicted from MS-derived parameters and DBH measured in the field. The linear regression showed a close agreement (R^2 = 0.82; RMSE = 4.36 cm) between MS predicted and observed DBH. However, the predicted DBH tends to overestimate (bias = 0.80%) the DBH slightly. The scatter plot and the regression statistics are shown in *Figure 28* and *Table 20*, respectively.

Table 20. Regression statistics of MS model validation.

r	R Square	Std. Error of the Estimate	RMSE	RMSE %	Bias	Bias %
0.906	0.820	4.333	4.361	14.291	0.244	0.801

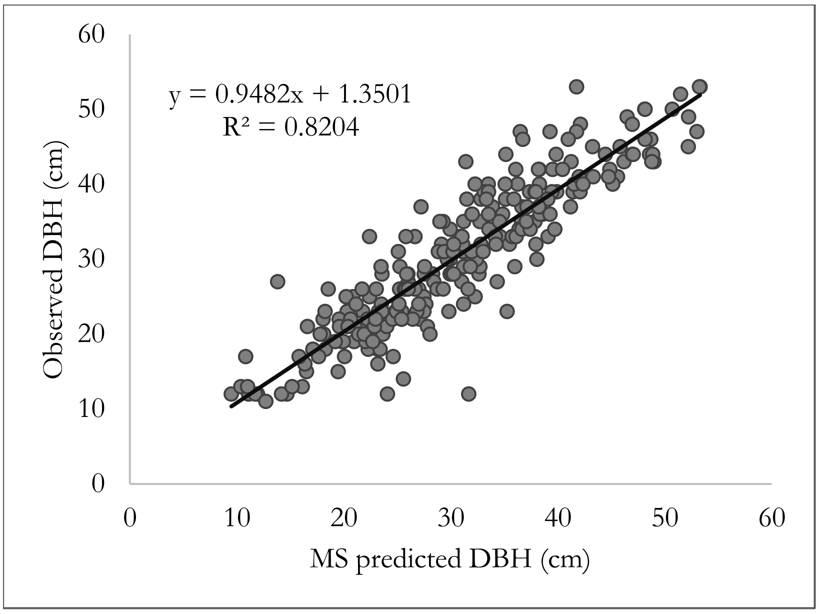

Figure 28. Scatter plot of field-measured DBH and DBH estimated using parameters derived from UAV MS imagery.

3.9.4. RGB model validation

A strong positive correlation (r = 0.90) was observed between DBH predicted from RGB-derived parameters and DBH measured in the field. The linear regression showed a close agreement (R2 = 0.80; RMSE = 4.54 cm) between RGB predicted and observed DBH. RGB predicted DBH was found slightly less accurate than MS predicted DBH using validation dataset. The scatter plot and the regression statistics of RGB model validation are shown in *Figure 29* and *Table 21*, respectively.

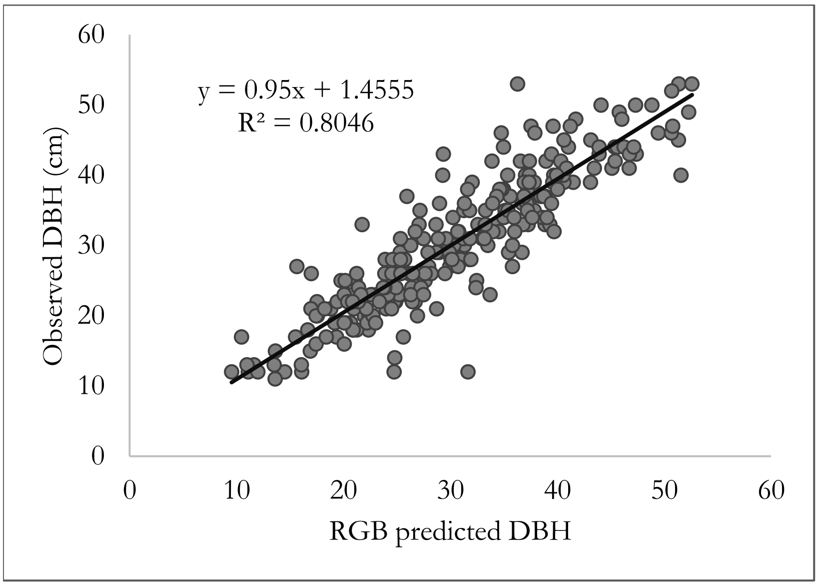

Figure 29. Scatter plot of field-measured DBH and DBH estimated using parameters derived from UAV RGB imagery.

Table 21. Regression statistics of RGB model validation.

r	R Square	Std. Error of the Estimate	RMSE	RMSE %	Bias	Bias %
0.897	0.805	4.520	4.537	14.869	0.076	0.247

3.9.5. DBH hypothesis testing

One-way ANOVA *F*-test showed no significant difference of mean DBH measured in the field and predicted using parameters derived from UAV MS and UAV RGB imagery ($F(2, 747) = 0.04$, $p > 0.05$). The test result is presented in *Table 22*.

Table 22. One-way ANOVA test of tree DBH.

SUMMARY						
Groups	**Count**	**Sum**	**Average**		**Variance**	
Field DBH (cm)	250	7629.00	30.52		104.15	
MS predicted DBH (cm)	250	7689.85	30.76		95.03	
RGB predicted DBH (cm)	250	7647.80	30.59		92.86	
ANOVA						
Source of Variation	**SS**	**df**	**MS**	**F**	**P-value**	**F crit**
Between Groups	7.77	2	3.88	0.04	0.96	3.01
Within Groups	72717.41	747	97.35			
Total	72725.17	749				

3.10. Plot-wise AGB

AGB was estimated using a species-specific allometric equation. The average AGB estimated from the field with LiDAR-measured parameter was 8.49 Mg plot^{-1} (i.e. 169.83 Mg ha^{-1}). On the other hand, the average AGB estimated from UAV-derived parameters of MS and RGB imagery was 8.68 and 9.06 Mg plot^{-1} (i.e. 173.52 and 181.24 Mg ha^{-1}), respectively (*Figure 30*). For all species, AGB estimated from UAV MS imagery was found less than the UAV RGB imagery. The minimum and maximum field with LiDAR-based AGB was 3.19 and 23.50 Mg plot^{-1} (i.e. 63.78 and 469.93 Mg ha^{-1}), respectively. On the contrary, the UAV MS and RGB AGB estimate ranged from 3.68-22.02 and 4.08-22.47 Mg plot^{-1} (i.e. 73.65-440.37 and 81.69-449.34 Mg ha^{-1}), respectively (*Appendix 5*).

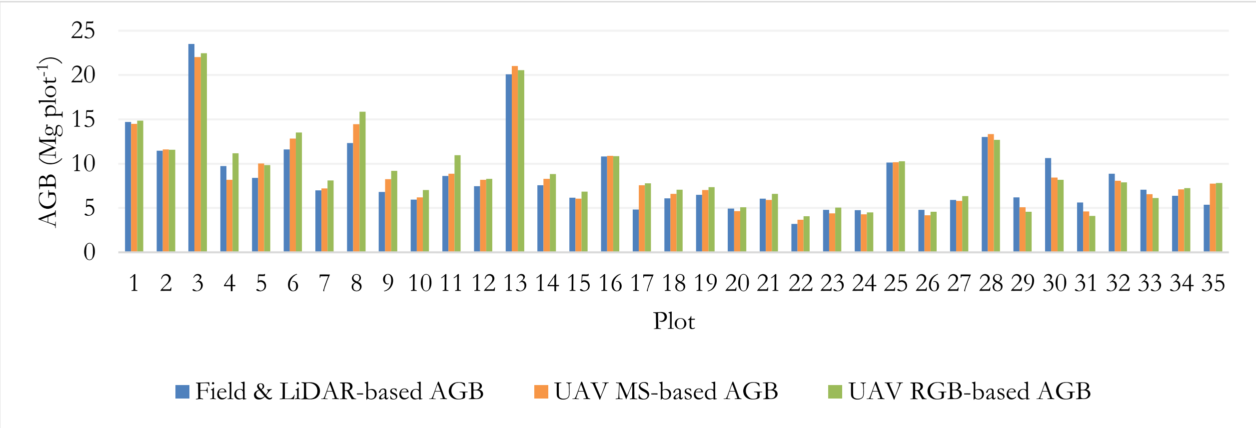

Figure 30. Plot-wise AGB estimated from the field with LiDAR and UAV-derived parameters.

3.10.1. AGB hypothesis testing

One-way ANOVA *F*-test showed no significant difference of mean AGB estimated from the field with LiDAR, UAV MS and UAV RGB-derived parameters ($F(2, 1887) = 0.69$, $p > 0.05$). The test result is shown in *Table 23*.

Table 23. One-way ANOVA test of AGB.

SUMMARY				
Groups	**Count**	**Sum**	**Average**	**Variance**
Field & LiDAR-based AGB	630	297207.49	471.76	238996.52
UAV MS-based AGB	630	303659.43	482.00	242088.61
UAV RGB-based AGB	630	317174.51	503.45	232307.34

ANOVA						
Source of Variation	**SS**	**df**	**MS**	**F**	**P-value**	**F crit**
Between Groups	329611.87	2	164805.94	0.69	0.50	3.00
Within Groups	4.49E+08	1887	237797.49			
Total	4.49E+08	1889				

3.11. Plot-wise AGC

The average AGC estimated from the field with LiDAR- measured parameter was 4.25 Mg plot^{-1} (i.e. 84.92 Mg ha^{-1}), while the average AGC estimated from UAV-derived parameters of MS and RGB imagery was 4.34 and 4.53 Mg plot^{-1} (i.e. 86.76 and 90.62 Mg ha^{-1}), respectively (*Figure 31*). The minimum and maximum field with LiDAR-based AGC was 1.59 and 11.75 Mg plot^{-1} (i.e. 31.89 and 234.97 Mg ha^{-1}), respectively, while MS and RGB-based AGC ranged from 1.84-11.01 and 2.04-11.23 Mg plot^{-1} (i.e. 36.83-220.19 and 40.84-224.67 Mg ha^{-1}), respectively (*Appendix 6*).

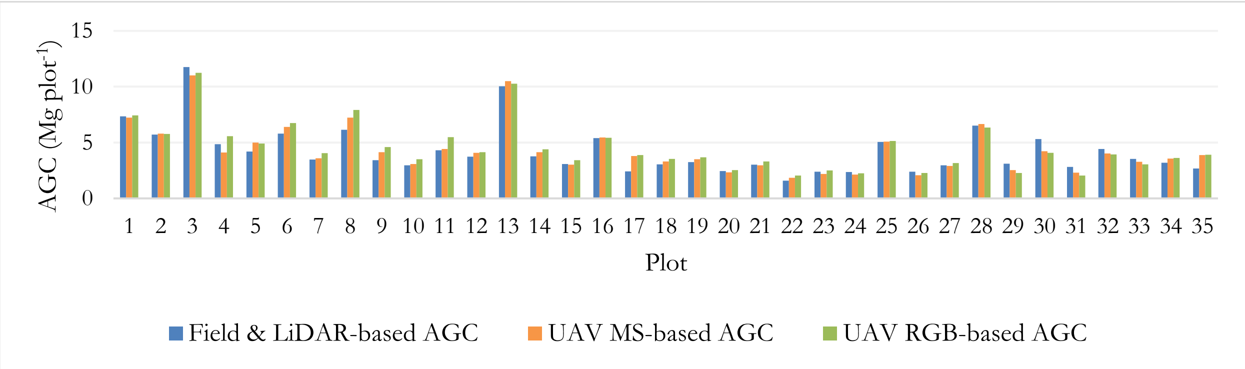

Figure 31. Plot-wise AGC estimated from the field with LiDAR and UAV-derived parameters.

3.12. Accuracy of AGB

3.12.1. Accuracy of UAV MS-based AGB

The AGB estimated from MS-derived parameters showed a close agreement (R^2 = 0.91; RMSE = 149.71 kg) with the field & LiDAR-based AGB. However, UAV MS estimated AGB tended to overestimate (bias = 2.17%). The scatter plot and regression statistics are presented in *Figure 32* and *Table 24*, respectively.

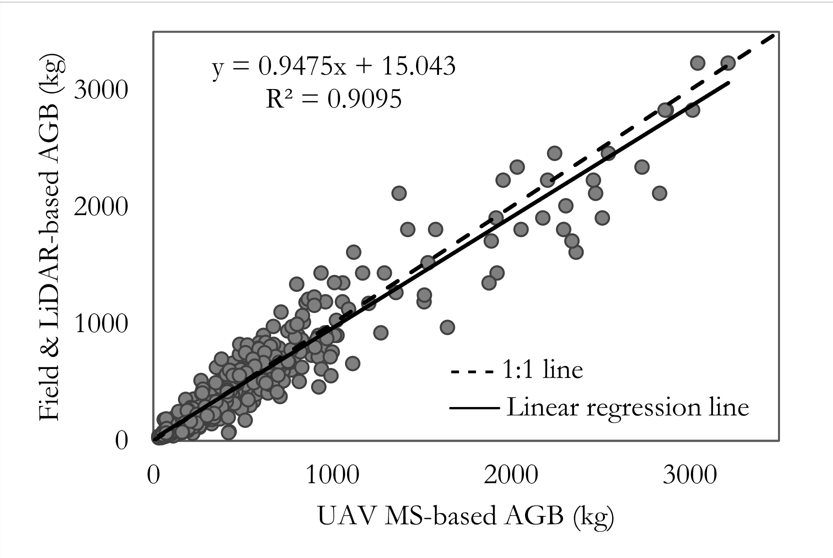

Figure 32. Scatter plot of the field with LiDAR-based AGB and UAV MS-based AGB.

Table 24. Regression statistics of the field with LiDAR-based and UAV MS-based AGB.

r	R^2	Std. Error of the Estimate	RMSE	RMSE %	Bias	Bias %
0.95	0.91	147.22	149.71	31.73	10.26	2.17

3.12.2. Accuracy of UAV RGB-based AGB

The AGB estimated from RGB-derived parameters showed a close agreement (R^2 = 0.89; RMSE = 166.85 kg) with the field & LiDAR-based AGB. However, UAV RGB estimated AGB tended to overestimate (bias = 6.73%). The accuracy of the RGB estimated AGB was lower than MS estimated AGB. The scatter plot and regression statistics are presented in *Figure 33* and *Table 25*, respectively.

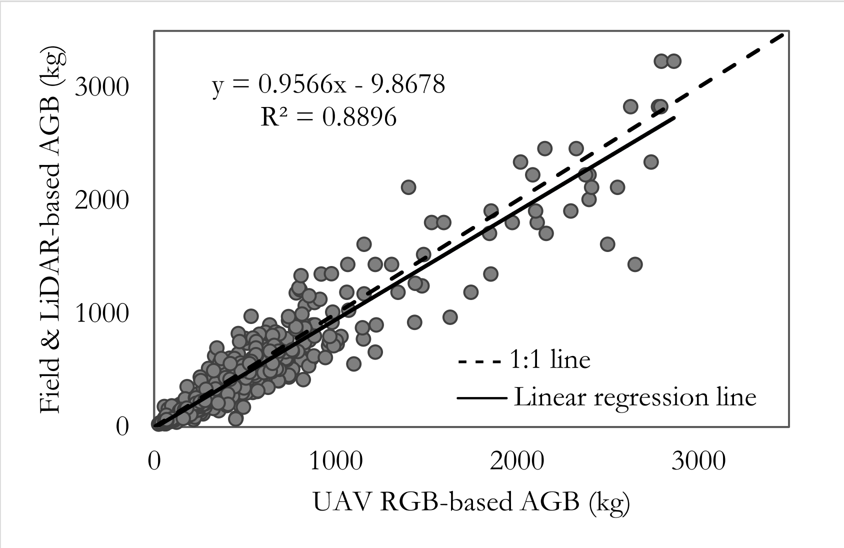

Figure 33. Scatter plot of the field with LiDAR-based AGB and UAV RGB-based AGB.

Table 25. Regression statistics of the field with LiDAR-based and UAV RGB-based AGB.

r	R Square	Std. Error of the Estimate	RMSE	RMSE %	Bias	Bias %
0.94	0.89	162.59	166.85	35.37	31.74	6.73

3.12.3. AGB hypothesis testing

Simple *t*-test of regression coefficient showed a significant relationship between estimated field with LiDAR-based AGB and UAV MS-based AGB (t = 79.42, df = 628, p < 0.05). Similarly, a significant relationship was observed between field with LiDAR-based AGB and UAV RGB-based AGB (t = 71.12, df = 628, p < 0.05). The test results are shown in *Table 26*.

Table 26. Simple t-test of regression models.

y	x	b_1	Std. Error	t	t crit	P-value
Field AGB	MS AGB	0.95	0.01	79.42	1.96	0.00
Field AGB	RGB AGB	0.96	0.01	71.12	1.96	0.00

4. DISCUSSION

4.1. Uncertainties of field-measured parameters

The field-measured DBH was slightly right-skewed (.346) (*Figure 11*) due to the exclusion of tress with DBH less than 10 cm as the reference parameter. Smaller trees (DBH < 10 cm) were omitted as they were less dominant in the study area and make no significant difference in AGB estimation (Gibbs et al., 2007). Measurement of tree DBH in the field was relatively easy and faster than tree height.

Tree height was measured in the field using laser distance meter, also known as laser ranger (Leica DISTO D510). The laser instrument has a tilt sensor that enables the measurement of both distance and angle within a specific range of accuracy. Tree height measurement in the field was most tricky as the laser instrument need to be targeted at the base and top of the tree. At the base point, the reflective laser target is required to measure the distance and tilt. However, the top point can be aimed with either pointfinder or crosshair without laser reflective target to measure the inclination. Targeting the base of the tree was straightforward. However, targeting treetop was often difficult due to occlusion and movement of treetops during the windy days. Since field-measured tree height was less accurate (*Figure 23*) due difficulty in seeing treetops, human bias and instrument error (Guerra-Hernández et al., 2017; Wallace et al., 2016), LiDAR-measured tree height was used as a reference data to assess the accuracy of UAV MS and RGB-derived tree height.

4.2. Quality of UAV point cloud

In this study, Pix4Dmapper was used to process the UAV images. The processing options, such as multiple image scale (half image size), optimal point density, and a minimum of three matches of keypoints, were used to generate the dense point cloud as considered by Guerra-Hernández et al. (2017). The average point cloud density for UAV MS and RGB imagery was 2.61 and 30.92 m^{-3}, respectively. The difference in point density is evident from transect profile shown in *Figure 34* and *Figure 35*. For instance, some part of the treetops in MS point cloud seems to be missing compared to RGB point cloud. Although both the MS sensor and RGB camera are passive sensors, the latter has more canopy penetration and better information on the forest floor. UAV MS imagery with lower spatial resolution compared to RGB imagery is associated with low point cloud density and less detailed information of the forest structure as reported by Shen et al. (2019). Studies have noted that the difference in point cloud density generated from UAV images using SfM approach may be attributed to image overlap, image resolution and algorithm used to create the point cloud (Dandois et al., 2015; Shen et al., 2019; White et al., 2013).

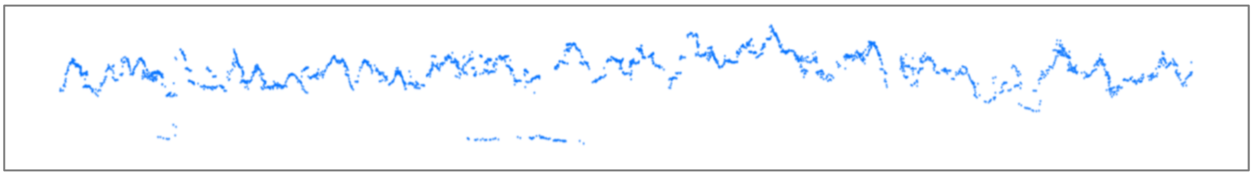

Figure 34. Transect profile of MS point cloud.

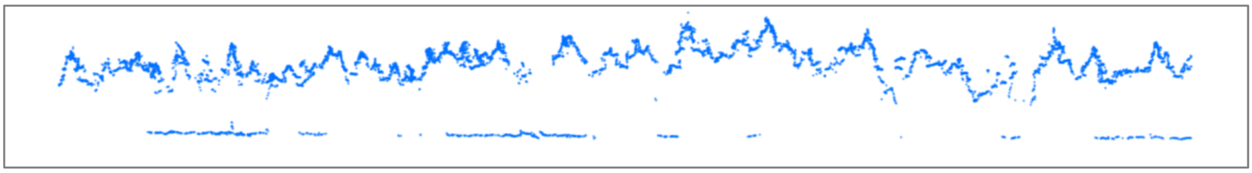

Figure 35. Transect profile of RGB point cloud.

4.3. Deriving crown diameter from the canopy projection area

In the field, the crown diameter can be determined by measuring the extent of the crown in N–S and E–W directions at the crown base (Grznárová et al., 2019; Pouliot et al., 2002). However, it is time-consuming and often challenging to determine the perimeter of the tree crown. Therefore, the crown diameter in this study was derived from CPA manually digitised from the UAV MS and RGB orthomosaic. Visually the MS-delineated tree crowns were less regular in shape compared to RGB CPA, which may be attributed to the different spectral resolution of the UAV MS and RGB images (*Figure 36*). However, there was no significant difference in mean crown diameter derived from UAV MS and RGB imagery. As expected, delineation of canopy outline was straightforward in MS orthomosaic for both isolated and clumped crowns compared to RGB orthomosaic due to high image contrast from NIR band.

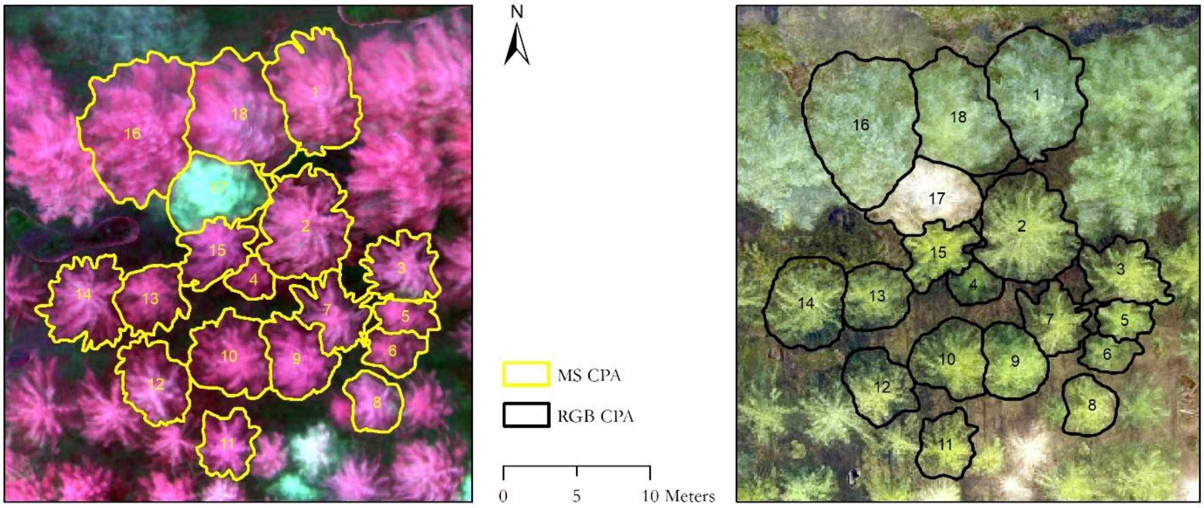

Figure 36. CPA digitised from UAV MS and RGB orthomosaic.

Previous studies have found high-resolution UAV RGB images suitable to retrieve the crown diameter (R^2 = 0.95, RMSE = 0.63 m) of conifer trees (Guerra-Hernández et al., 2016). Having no significant difference in mean crown diameter (*Table 9*) and strong positive correlation (*Figure 19*) between UAV MS and RGB-derived crown diameter suggest the suitability of retrieving tree crown information from UAV MS imagery. Crown size information derived from UAV imagery has been applied to quantify defoliation in a mix pine-oak forest (Cardil et al., 2019). Moreover, such information can be valuable for forest management practices such as thinning to enhance tree growth rate (Shimano, 1997).

4.4. Tree height accuracy

Tree height derived from MS CHM (R^2 = 0.79, RMSE 1.94 m) and RGB CHM (R^2 = 0.83, RMSE = 2.95 m) showed good agreement with tree height derived from LiDAR. The accuracy of tree height derived from MS and RGB CHM were higher than the result of Panagiotidis et al. (2017). They achieved reasonable accuracy of conifer tree heights (RMSE = 3 m) derived from UAV CHM. The considerable variation of UAV CHM and LiDAR-derived tree height from this study is consistent with tree height derived from UAV CHM (Iizuka et al., 2017), UAV point cloud (Wallace et al., 2016), and ALS (Bazezew et al., 2018; Hopkinson et al., 2008) point cloud data. However, the accuracy of this study is lower than that obtained by previous studies using UAV (Birdal et al., 2017; Guerra-Hernández et al., 2016; Guerra-Hernández et al., 2017; Krause et al., 2019; Lin et al., 2018; Zainuddin et al., 2016) and LiDAR (Heurich et al., 2004; Holmgren, 2004; Kwak et al., 2007) data, especially in a conifer forest stand.

The accuracy of tree height estimated from RGB CHM (R^2 = 0.83) was higher than tree height estimated from MS CHM (R^2 = 0.79). The higher accuracy may be attributed to high image overlap and image resolution as outlined in Dandois et al. (2015), thereby affecting the generation of point cloud density, DSM and DTM. For instance, the critical information on the part of tree such as treetops is less pronounced in MS DSM compared to RGB DSM (*Figure 37*). As a result, tree height from MS CHM (bias = 2.90%) tended to overestimate less than tree height from RGB CHM (bias = 12.33%). On the contrary, the deviation of estimated RGB-derived (RMSE = 2.95 m) tree height was higher than MS-derived tree height (RMSE = 1.94 m) when they were compared with reference tree height from LiDAR. The higher deviation is attributed to image resolution and time difference in the collection of LiDAR and UAV images. LiDAR and UAV images were collected in February 2019 and February - March 2020, respectively. Increase in tree height due to time difference seems to be captured explicitly by the UAV RGB images due to high spatial resolution.

RGB CHM-derived tree height was higher than MS CHM-derived tree height. Shen et al. (2019) observed a similar result in assessing the tree height derived from the SfM point cloud of UAV MS and RGB imagery. In the vegetated area, both MS and RGB DTM seems to vary by a few meters. However, on average, MS DTM is slightly elevated than RGB DTM (~ 1 m difference). Nevertheless, MS and RGB DTM were found in close agreement in the area with less or no vegetation.

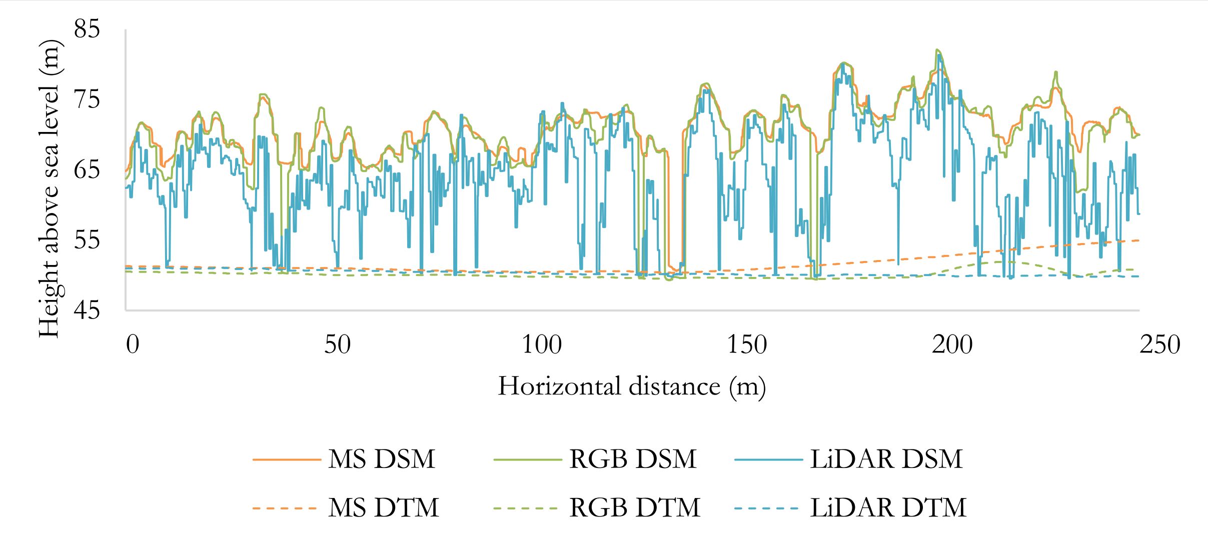

Figure 37. Transect profiles of MS, RGB and LiDAR-derived height models.

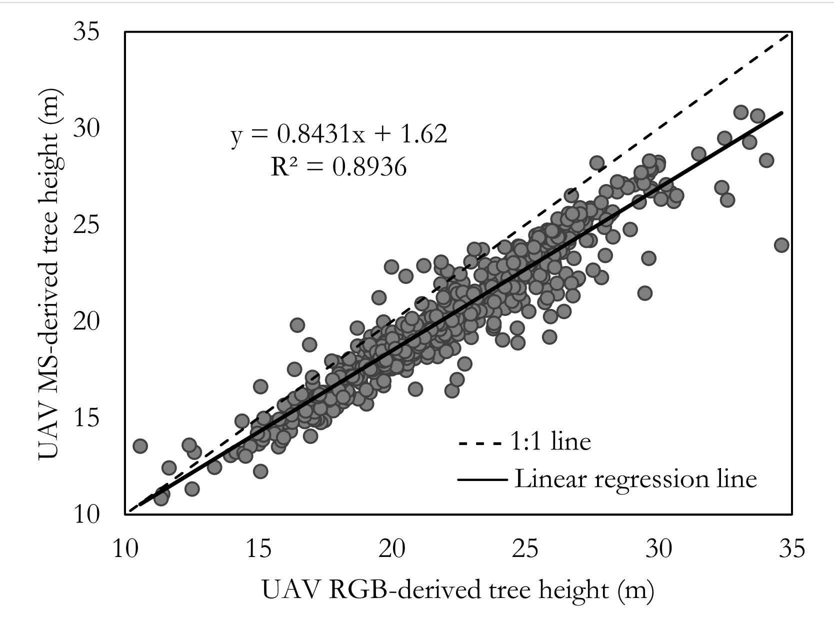

Figure 38. Scatter plot of UAV MS and RGB-derived tree height.

Although there is a slight variation in DSM and DTM generated from UAV images, the tree height estimated from MS CHM showed high consistency ($R^2 = 0.89$) with the tree height estimated from RGB CHM (*Figure 38*). The R^2 from this study is comparable with the result from Shen et al. (2019), who reported a strong correlation ($R^2 = 0.75–0.94$) of tree height derived from MS and RGB point cloud. The tree height generated from MS CHM was on average (~ 2 m) shorter than tree height generated from RGB CHM. Tree height information retrieved from UAV images is crucial for forest management practices such as tree growth monitoring and sustainable timber production.

4.5. Estimating tree DBH from UAV imagery

Studies have found a strong correlation between DBH and crown size measured in the field (Gonzalez-Benecke et al., 2014; Hemery et al., 2005; Shimano, 1997). Since the crown size information can be retrieved from remotely sensed images, such relationships provide the basis to estimate DBH. In this study, *TH* × *CD* was a good model, if not the best, to predict DBH (*Table 16*, *Table 18*). Jucker et al. (2017) found that *TH* × *CD* ($R^2 = 0.70$) as a compound variable performing better in estimating DBH compared to the model with tree height ($R^2 = 0.56$) and crown diameter ($R^2 = 0.31$) as a separate predictor. The reason may be that the compound variable complements each other in predicting the stem diameter more accurately. Trees usually grow faster at an early stage to compete for the light and escape understory shade attaining the maximum height, while the stem diameter continues to grow at all stages (King, 2005; Sterck & Bongers, 2001). In such a case, estimating the stem diameter from tree height alone becomes problematic since trees with similar height may have varying DBH. Therefore, information on crown size becomes crucial in differentiating trees of similar height with different stem size (Gonzalez-Benecke et al., 2014; Jucker et al., 2017; King, 2005). The result of this study, therefore, highlights the importance of both tree height and crown size required to estimate DBH.

MS model performed better than the RGB model in estimating trees DBH, although the residual plot showed a similar pattern without a clear trend of either underestimation or overestimation of tree DBH (*Figure 39*). The result of the both MS ($R^2 = 0.82$, RMSE = 4.36 cm) and RGB ($R^2 = 0.80$, RMSE = 4.54 cm) model validation from this study is higher to that reported by Jucker et al. (2017), who used tree height and crown diameter from LiDAR to estimate stem diameter (RMSE = 9.7 cm; bias = -1.2%). Guerra-Hernández et al. (2017) used UAV-derived tree height and crown area to model DBH and obtained comparable accuracy ($R^2 = 0.79$, RMSE = 2.36 cm). Popescu (2007) and Heurich et al. (2004) obtained 87% and 85% of observed DBH variance explained by ALS-derived tree height and crown diameter with RMSE of 4.9 and 6.8 cm, respectively. Morevoer, Zhao et al. (2009) obtained slightly higher accuracy of DBH predicted from tree height, crown diameter, and crown based height in a conifer forest. Nevertheless, the estimation of DBH in this study performed well considering RMSE, although the R^2 was slightly higher in some studies (Heurich et al., 2004; Popescu, 2007; Zhao et al., 2009).

The estimation of mean DBH from UAV-derived parameters was not significantly different from the DBH measured in the field. The result of this study highlights the feasibility of estimating stem diameter from UAV MS-derived parameters such as tree height and crown diameter in a managed conifer forest. Deriving relationship between DBH and crown structure has several important implications such as assessment of forest biomass and carbon stock and understanding the complex forest dynamics (Jucker et al., 2017). Also, DBH information can be used as an input for tree allometry and forest stock assessment (Holmgren, 2004).

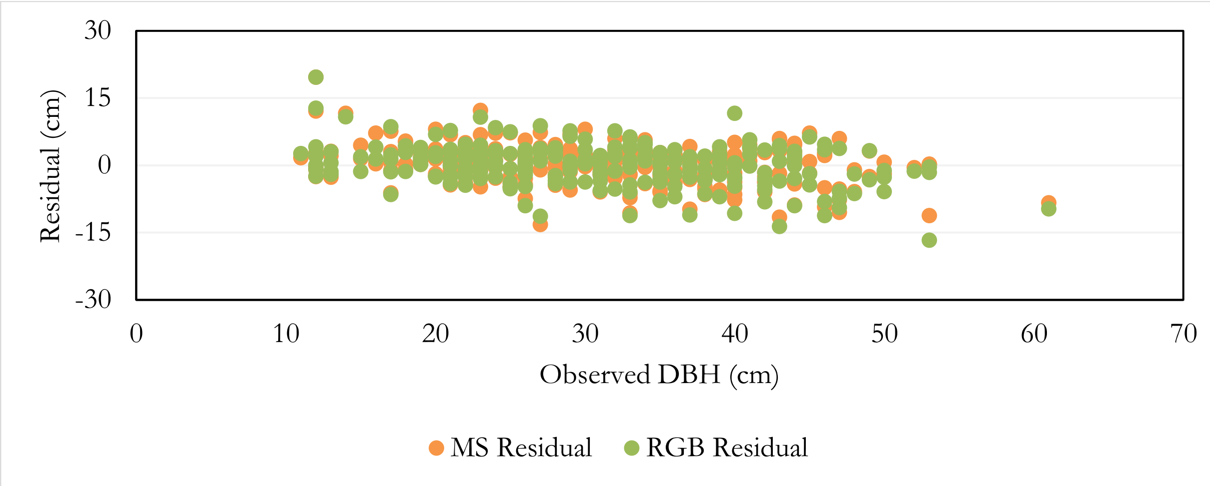

Figure 39. Residual plot of UAV MS and RGB DBH model validation.

4.6. AGB

One-way ANOVA *F*-test showed no significant difference in mean AGB, thereby failing to reject the null hypothesis. The results of this study demonstrate that UAV MS imagery is suitable for estimating AGB and carbon stock in a managed coniferous forest. Since the study area have a mix of both young and matured stand, there is a considerable variation in the estimated AGB. For instance, the field with LiDAR-based AGB at tree level ranged from 33 to 3973 Kg, while MS and RGB AGB ranged from 22 to 3748 kg and 21 to 3942 kg, respectively. The estimate of this study is comparable with the result of Popescu (2007), whose estimate ranged from 13.02 to 3254 kg in pine trees (DBH = 8-78 cm, tree height = 9-37 m).

To compare the estimated AGB with related studies, the plot level AGB was extrapolated to hectare level (*Figure 40*). At hectare level, the average field with LiDAR-based AGB was 169.83 Mg ha^{-1}, while MS and RGB-based AGB were 173.52 and 181.24 Mg ha^{-1}, respectively. The estimated AGB of this study is higher than that of Primasatya et al. (2016) in the evergreen forest (AGB = 131 Mg ha^{-1}) in the same study area assessed in 2015 using a terrestrial laser scanner. Solberg et al. (2010) found the maximum AGB up to 355 Mg ha^{-1} estimated using the allometric equation in Norway spruce and Scots pine forest with minimum and maximum tree height of 7.6 and 31.3 m, respectively. The maximum AGB estimate of this study was higher (470 Mg ha^{-1}) with tree height ranging from 6 to 35 m in a mixed conifer forest.

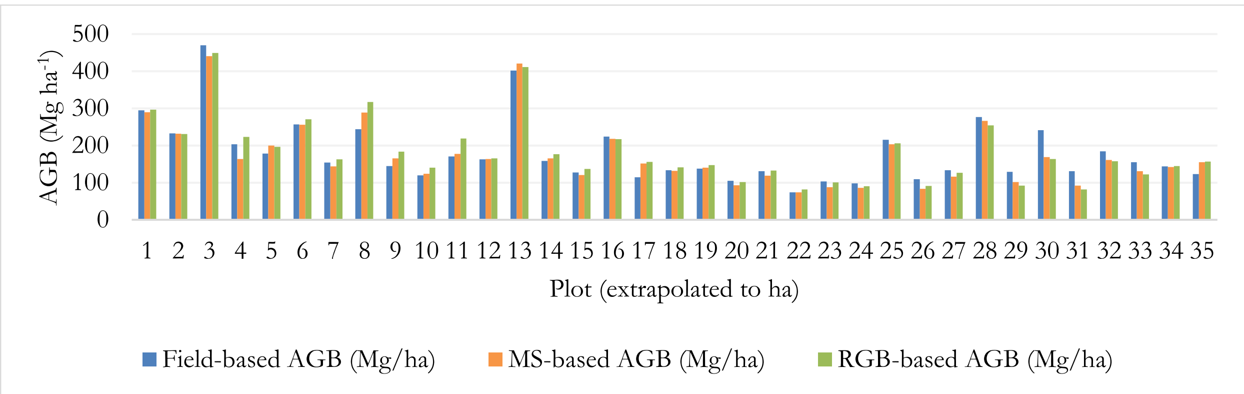

Figure 40. Plot-wise AGB extrapolated to hectare level.

Accurate and up to date information on forest biomass and carbon stock is essential for various current and future policy initiatives related to the UNFCCC. For instance, the Paris Agreement on Climate Change requires ratifying countries to report changes in forest biomass and carbon stocks under afforestation, reforestation and forest management in Article 3.3 and 3.4 (UNFCCC, 2008). Also, it is essential to monitor

Goal 15 (Life on land) of the United Nations Sustainable Development Goals (SDGs), and particularly the indicator concerning the implementation of sustainable forest management (United Nations, 2015).

4.7. AGB accuracy

As hypothesised, the accuracy of estimated MS AGB (R^2 = 0.91, RMSE = 149.71 kg) was higher than RGB AGB (R^2 = 0.89, RMSE = 166.85 kg) when they are assessed using field with LiDAR-based AGB. The higher accuracy of MS AGB is attributed to higher accuracy of DBH modelled from MS-derived parameters. Although the accuracy of tree heights may have affected the accuracy of AGB estimate using an allometric equation, the influence is typically not as pronounced as DBH. The result of this study is better than Jucker et al. (2017), who used ALS-derived parameters to predict DBH and estimate AGB (RMSE = 0.86 Mg, bias = 27.7%). However, it is similar to that of Popescu (2007) (R^2 = 0.88, RMSE = 162.72 kg), and slightly better than Zhao et al. (2009) (R^2 = 0.80, RMSE = 237 kg), who used ALS-derived parameters to estimate AGB. Moreover, the result of this study is comparable with Guerra-Hernández et al. (2017), who used UAV-derived tree height and crown area to estimate AGB (R^2 = 0.84, RMSE = 117.8 kg). However, the accuracy of the AGB reported by Lin et al. (2018) was slightly better (R^2 = 0.96, RMSE = 54.90 kg) in a sparse coniferous forest.

The accuracy of estimated AGB was examined at hectare level to compare with related studies (*Figure 41*). As expected, the accuracy of estimated MS (R^2 = 0.94, RMSE = 21.97 Mg) and RGB (R^2= 0.91, RMSE = 28.61 Mg) AGB was higher at hectare level compared to tree level. The result of this study is similar with Zhao et al. (2009) and Ota et al. (2015), who obtained R^2 = 0.94, RMSE = 14.4 Mg ha^{-1}, and R^2 = 0.76, RMSE = 51.79 Mg ha^{-1}, respectively. The comparable result (R^2 = 0.91, RMSE = 19 Mg ha^{-1}) was also obtained by Solberg et al. (2010) using parameters derived from the ALS point cloud.

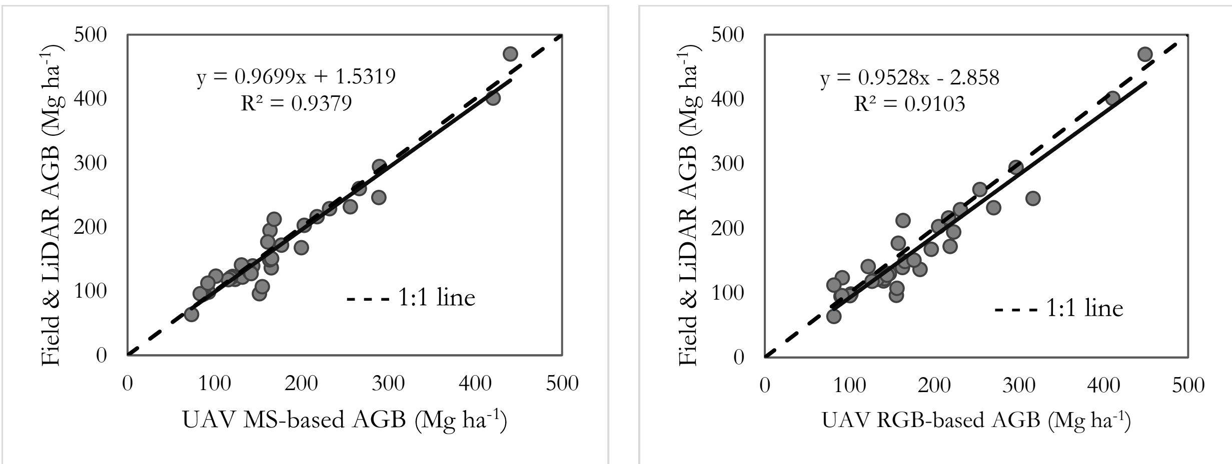

a) Field with LiDAR-based AGB and UAV MS-based AGB at hectare level.

b) Field with LiDAR-based AGB and UAV RGB-based AGB at hectare level.

Figure 41. Scatter plot of the field with LiDAR-based and UAV MS and RGB-based AGB.

It is important to note that the AGB estimated from MS-derived parameters were in close agreement with AGB estimated from RGB-derived parameters (*Figure 42*). Moreover, the consistency (R^2) of estimated AGB was similar at both tree and hectare level. Therefore, the results of this study demonstrate that individual tree parameters (*TH, DBH, AGB*) could be estimated from very high-resolution UAV MS imagery in a managed mixed conifer forest, suggesting promising application for REDD+ monitoring and forest management practices at a local scale.

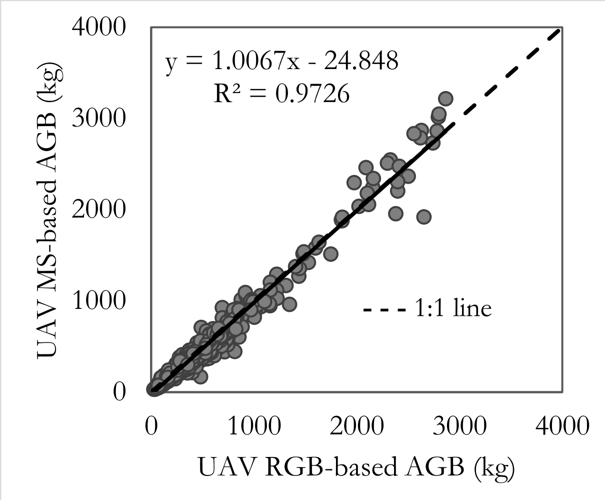

a) MS and RGB-based AGB at tree level.

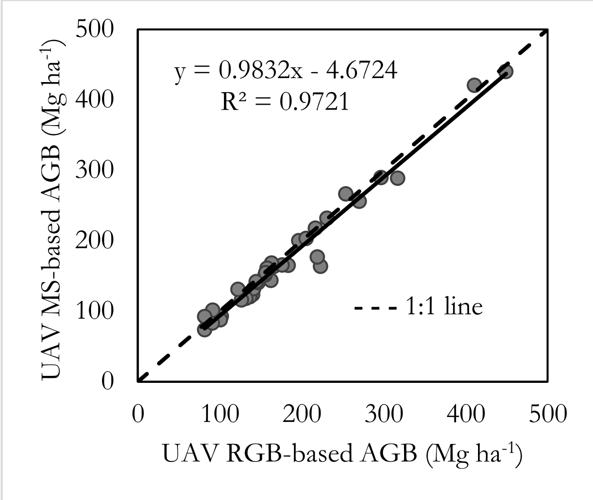

b) MS and RGB-based AGB at hectare level.

Figure 42. Scatter plot of UAV MS and RGB-based estimated AGB.

4.8. Limitation

In this study, only the trees with DBH of more than 10 cm were considered for AGB estimation. Although studies have noted that trees less than 10 cm have a negligible contribution to AGB, exclusion of trees less than 10 cm in a forest stand predominantly with young trees can have a significant effect. Moreover, the exclusion of young and undetected understory can result in higher accuracy of remotely sensed tree parameters.

Measuring crown diameter in the field is time-consuming and often a challenging task. Therefore, this study has derived the tree crown parameter from UAV orthomosaics using manual on-screen digitisation. Studies have used manually digitised crown as reference data to assess the accuracy of tree crown delineated using algorithms such as inverse watershed segmentation, object-based image analysis, and region growing, to name a few. Although manually digitised tree crowns are often considered as most accurate, it has errors associated with human bias. Despite the challenges of measuring a crown diameter in the field, this study recommends measuring a few dominant trees in the plot to assess the accuracy of crown diameter derived from UAV images.

Flight parameters used to acquire UAV MS, and RGB images were slightly different. Using same flight parameters as that of the multispectral sensor to capture UAV RGB images had an issue of uncalibrated images during image processing in Pix4Dmapper. The option to overcome the uncalibrated images was to either increase the fly height or an image overlap. Since the fly height was restricted to 120 m, the overlap of RGB flight was parameterised to 90% to obtain the desired output. Therefore, this study recommends a double grid mission with high overlap, preferably ≥ 90% to overcome such problem in a dense forest. A species-specific allometric equation was used to estimate AGB. Using an allometric equation different from this study may result in the different estimation of AGB/AGC.

5. CONCLUSION

The study concluded multispectral sensor UAV imagery suitable for estimating AGB/AGC. The accuracy of estimated AGB/AGC using UAV MS-derived tree parameter was found slightly more accurate than UAV RGB-derived tree parameter. Therefore, UAV MS imagery would be helpful to provide more accurate information on AGB/AGC for reporting national GHG accounting and REDD+ monitoring. Accurate and up to date information on biomass is also essential for Goal 15 of the United Nations SDGs, and particularly to monitor progress towards sustainable forest management (United Nations, 2015).

UAV MS orthomosaic with a high spectral resolution facilitated a straightforward delineation of CPA using on-screen manual digitisation compared to UAV RGB orthomosaic. However, a strong positive correlation (R^2 = 0.96) and the insignificant difference between UAV MS and RGB-derived crown diameter indicates their ability to estimate comparable DBH. Also, crown size information derived from UAV imagery can be useful to quantify defoliation in a forest (Cardil et al., 2019), and support forest management practices such as thinning (Shimano, 1997).

Field-measured and UAV-derived tree height had lower agreement than LiDAR and UAV-derived tree height. Also, a high agreement was found between the UAV MS and RGB-derived tree height. Therefore, SfM technique used to generate a point cloud that produces DSM and DTM to derive UAV CHM-based tree height in a managed conifer forest appears to be more reliable than the tree height measured in the field due to human bias and instrument error. Using LiDAR-measured tree height as a reference data, UAV RGB-derived (R^2 = 0.83) tree height was slightly more accurate than UAV MS-derived tree height (R^2 = 0.79). A significant difference of mean tree height was found between all groups which may be attributed to a different spatial resolution of UAV MS and UAV RGB images besides time difference in the collection of UAV and LiDAR data. Nevertheless, tree height information derived from UAV images is crucial for forest management practices such as tree growth monitoring and sustainable timber production.

To estimate DBH, UAV MS model (R^2 = 0.82, RMSE = 4.36) was slightly more accurate than UAV RGB model (R^2 = 0.81, RMSE = 4.54). However, there was no significant difference in mean DBH measured in the field and predicted using parameters derived from the UAV MS and RGB imagery. Therefore, UAV MS imagery can be used to estimate DBH to complement traditional forest inventory which is expensive and time-consuming. DBH is one of the essential parameters for tree allometry and forest stock assessment.

At the plot level, mean AGB assessed from the field with LiDAR-measured parameter using species-specific allometric equation was less than mean AGB estimated from UAV MS and RGB imagery. There was no significant difference of mean AGB estimated from UAV MS, UAV RGB, and field with LiDAR-derived parameter. However, the accuracy of UAV MS-based AGB (R^2 = 0.91, RMSE = 149.71 kg) was higher than UAV RGB-based AGB (R^2 = 0.89, RMSE = 166.85 kg) when they were assessed using field with LiDAR-based AGB at tree level. Therefore, the result of this study shows that UAV MS imagery is suitable for REDD+ monitoring and forest management practices in a managed coniferous forest at a local scale.

LIST OF REFERENCES

Baccini, A., Laporte, N., Goetz, S. J., Sun, M., & Dong, H. (2008). A first map of tropical Africa's above-ground biomass derived from satellite imagery. *Environmental Research Letters*, *3*(4), 045011. https://doi.org/10.1088/1748-9326/3/4/045011

Balsi, M., Esposito, S., Fallavollita, P., & Nardinocchi, C. (2018). Single-tree detection in high-density LiDAR data from UAV-based survey. *European Journal of Remote Sensing*, *51*(1), 679–692. https://doi.org/10.1080/22797254.2018.1474722

Bartelink, H. H. (1996). Allometric relationships on biomass and needle area of Douglas-fir. *Forest Ecology and Management*, *86*(1–3), 193–203. https://doi.org/10.1016/S0378-1127(96)03783-8

Bazezew, M. N., Hussin, Y. A., & Kloosterman, E. H. (2018). Integrating airborne LiDAR and terrestrial laser scanner forest parameters for accurate above-ground biomass/carbon estimation in Ayer Hitam tropical forest, Malaysia. *International Journal of Applied Earth Observation and Geoinformation*, *73*, 638–652. https://doi.org/10.1016/j.jag.2018.07.026

Berhe, T. H. (2018). *Towards a UAV based standalone system for estimating and mapping above ground biomass/ carbon stock in Berkelah tropical rain forest, Malaysia* (Master's Thesis). Retrieved from https://library.itc.utwente.nl/login/2018/msc/nrm/berhe.pdf

Birdal, A. C., Avdan, U., & Türk, T. (2017). Estimating tree heights with images from an unmanned aerial vehicle. *Geomatics, Natural Hazards and Risk*, *8*(2), 1144–1156. https://doi.org/10.1080/19475705.2017.1300608

Cardil, A. I., Otsu, K. I., Pla, M., Alberto Silva, C., & Brotons, L. (2019). Quantifying pine processionary moth defoliation in a pine-oak mixed forest using unmanned aerial systems and multispectral imagery. *PloS One*, *14*(3). https://doi.org/10.1371/journal.pone.0213027

Carvajal-Ramírez, F., Marques da Silva, J. R., Agüera-Vega, F., Martínez-Carricondo, P., Serrano, J., & Moral, F. J. (2019). Evaluation of fire severity indices based on pre- and post-fire multispectral imagery sensed from UAV. *Remote Sensing*, *11*(9), 993. https://doi.org/10.3390/rs11090993

Carvajal-Ramírez, F., Serrano, J. M. P. R., Agüera-Vega, F., & Martínez-Carricondo, P. (2019). A comparative analysis of phytovolume estimation methods based on UAV-photogrammetry and multispectral imagery in a Mediterranean forest. *Remote Sensing*, *11*(21), 2579. https://doi.org/10.3390/rs11212579

Chai, T., & Draxler, R. R. (2014). Root mean square error (RMSE) or mean absolute error (MAE)? – Arguments against avoiding RMSE in the literature. *Geoscientific Model Development*, *7*(3), 1247–1250. https://doi.org/10.5194/gmd-7-1247-2014

Cienciala, E., Černý, M., Tatarinov, F., Apltauer, J., & Exnerová, Z. (2006). Biomass functions applicable to Scots pine. *Trees*, *20*(4), 483–495. https://doi.org/10.1007/s00468-006-0064-4

Colomina, I., & Molina, P. (2014). Unmanned aerial systems for photogrammetry and remote sensing: A review. *ISPRS Journal of Photogrammetry and Remote Sensing*, *92*, 79–97. https://doi.org/10.1016/j.isprsjprs.2014.02.013

Cooper, R. J. (2003). World markets for coniferous forest products: Recent trends and future prospects. *Acta Horticulturae*, *615*, 349–353. https://doi.org/10.17660/ActaHortic.2003.615.37

Dandois, J., Olano, M., & Ellis, E. (2015). Optimal altitude, overlap, and weather conditions for computer vision UAV estimates of forest structure. *Remote Sensing*, *7*(10), 13895–13920. https://doi.org/10.3390/rs71013895

Dash, J. P., Pearse, G. D., & Watt, M. S. (2018). UAV multispectral imagery can complement satellite data for monitoring forest health. *Remote Sensing*, *10*(8), 1216. https://doi.org/10.3390/rs10081216

Dormann, C. F., Elith, J., Bacher, S., Buchmann, C., Carl, G., Carré, G., … Lautenbach, S. (2013). Collinearity: a review of methods to deal with it and a simulation study evaluating their performance. *Ecography*, *36*(1), 27–46. https://doi.org/10.1111/j.1600-0587.2012.07348.x

Duncanson, L., Armston, J., Disney, M., Avitabile, V., Barbier, N., Calders, K., … Williams, M. (2019). The importance of consistent global forest aboveground biomass product validation. *Surveys in Geophysics*, *40*(4), 979–999. https://doi.org/10.1007/s10712-019-09538-8

Farjon, A. (2018). The kew review: Conifers of the world. *Kew Bulletin*, *73*(1), 1–16. https://doi.org/10.1007/s12225-018-9738-5

Fehrmann, L., & Kleinn, C. (2006). General considerations about the use of allometric equations for biomass estimation on the example of Norway spruce in central Europe. *Forest Ecology and Management*, *236*(2–3), 412–421. https://doi.org/10.1016/j.foreco.2006.09.026

Fernández-Guisuraga, J., Sanz-Ablanedo, E., Suárez-Seoane, S., & Calvo, L. (2018). Using unmanned aerial vehicles in postfire vegetation survey campaigns through large and heterogeneous areas: Opportunities and challenges. *Sensors*, *18*(2), 586. https://doi.org/10.3390/s18020586

Gibbs, H. K., Brown, S., Niles, J. O., & Foley, J. A. (2007). Monitoring and estimating tropical forest carbon stocks: Making REDD a reality. *Environmental Research Letters*, *2*(4), 045023. https://doi.org/10.1088/1748-9326/2/4/045023

Gini, R., Passoni, D., Pinto, L., & Sona, G. (2014). Use of unmanned aerial systems for multispectral survey and tree classification: A test in a park area of northern Italy. *European Journal of Remote Sensing*, *47*(1), 251–269. https://doi.org/10.5721/EuJRS20144716

Gonzalez-Benecke, C. A., Gezan, S. A., Samuelson, L. J., Cropper, W. P., Leduc, D. J., & Martin, T. A. (2014). Estimating Pinus palustris tree diameter and stem volume from tree height, crown area and stand-level parameters. *Journal of Forestry Research*, *25*(1), 43–52. https://doi.org/10.1007/s11676-014-0427-4

González-Jaramillo, V., Fries, A., & Bendix, J. (2019). AGB estimation in a tropical mountain forest (TMF) by means of RGB and multispectral images using an unmanned aerial vehicle (UAV). *Remote Sensing*, *11*(12), 1413. https://doi.org/10.3390/rs11121413

Grznárová, A., Mokroš, M., Surový, P., Slavík, M., Pondelík, M., & Merganič, J. (2019). The crown diameter estimation from fixed wing type of UAV imagery. *International Archives of the Photogrammetry, Remote Sensing & Spatial Information Sciences*, 337–341. https://doi.org/10.5194/isprs-archives-XLII-2-W13-337-2019

Guerra-Hernández, J, González-Ferreiro, E., Sarmento, A., Silva, J., Nunes, A., Correia, A. C., … Díaz-Varela, R. (2016). Using high resolution UAV imagery to estimate tree variables in Pinus pinea plantation in Portugal. *Forest Systems*, *25*(2), 9. https://doi.org/10.5424/fs/2016252-08895

Guerra-Hernández, Juan, González-Ferreiro, E., Monleón, V., Faias, S., Tomé, M., & Díaz-Varela, R. (2017). Use of multi-temporal UAV-derived imagery for estimating individual tree growth in Pinus pinea stands. *Forests*, *8*(8), 300. https://doi.org/10.3390/f8080300

Hashem, M. A. (2019). *Estimation of aboveground biomass/ carbon stock and carbon sequestration using UAV imagery at Kebun Raya Unmul Samarinda education forest, East Kalimantan, Indonesia* (Master's Thesis). Retrieved from https://library.itc.utwente.nl/papers_2019/msc/nrm/hashem.pdf

Hemery, G. E., Savill, P. S., & Pryor, S. N. (2005). Applications of the crown diameter-stem diameter relationship for different species of broadleaved trees. *Forest Ecology and Management*, *215*(1–3), 285–294. https://doi.org/10.1016/j.foreco.2005.05.016

Herold, M., Carter, S., Avitabile, V., Espejo, A. B., Jonckheere, I., Lucas, R., … De Sy, V. (2019). The role and need for space-based forest biomass-related measurements in environmental management and policy. *Surveys in Geophysics*, *40*(4), 757–778. https://doi.org/10.1007/s10712-019-09510-6

Heurich, M., Persson, Å., Holmgren, J., & Kennel, E. (2004). Detecting and measuring individual trees with laser scanning in mixed mountain forest of central Europe using an algorithm developed for Swedish boreal forest conditions. *International Archives of Photogrammetry, Remote Sensing and Spatial Information Sciences*, *36*(8), 307–312.

Hirata, Y., Takao, G., Sato, T., & Toriyama, J. (2012). *REDD-plus Cookbook*. REDD Research and Development Center, Forestry and Forest Products Research Institute Japan. Retrieved from https://www.ffpri.affrc.go.jp/redd-rdc/en/reference/cookbook/redd_cookbook_all_high_en.pdf

Hirt, C. (2014). Digital terrian models. In E. Grafarend (Ed.), *Encyclopedia of geodesy* (pp. 1–6). Cham: Springer. https://doi.org/10.1007/978-3-319-02370-0_31-1

Holmgren, J. (2004). Prediction of tree height, basal area and stem volume in forest stands using airborne laser scanning. *Scandinavian Journal of Forest Research*, *19*(6), 543–553. https://doi.org/10.1080/02827580410019472

Hopkinson, C., Chasmer, L., & Hall, R. J. (2008). The uncertainty in conifer plantation growth prediction from multi-temporal lidar datasets. *Remote Sensing of Environment*, *112*(3), 1168–1180. https://doi.org/10.1016/j.rse.2007.07.020

Houghton, R. A., Hall, F., & Goetz, S. J. (2009). Importance of biomass in the global carbon cycle. *Journal of Geophysical Research: Biogeosciences*, *114*(G2). https://doi.org/10.1029/2009JG000935

Huang, X., Ziniti, B., Torbick, N., & Ducey, M. (2018). Assessment of forest above ground biomass estimation using multi-temporal C-band Sentinel-1 and polarimetric L-band PALSAR-2 data. *Remote Sensing*, *10*(9), 1424. https://doi.org/10.3390/rs10091424

Iglhaut, J., Cabo, C., Puliti, S., Piermattei, L., O'Connor, J., & Rosette, J. (2019). Structure from motion photogrammetry in forestry: A review. *Current Forestry Reports*, *5*(3), 155–168. https://doi.org/10.1007/s40725-019-00094-3

Iizuka, K., Yonehara, T., Itoh, M., & Kosugi, Y. (2017). Estimating tree height and diameter at breast height (DBH) from digital surface models and orthophotos obtained with an unmanned aerial system for a Japanese cypress (Chamaecyparis obtusa) forest. *Remote Sensing*, *10*(2), 13. https://doi.org/10.3390/rs10010013

IPCC. (2003). *Good practice guidance for land use, land use change and forestry*. Retrieved from http://www.ipcc-nggip.iges.or.jp

IPCC. (2007). *Climate change 2007 synthesis report*. Retrieved from https://www.ipcc.ch/site/assets/uploads/2018/02/ar4_syr_full_report.pdf

Jagodziński, A., Dyderski, M., Gęsikiewicz, K., & Horodecki, P. (2018). Tree- and stand-level biomass estimation in a Larix decidua Mill. Chronosequence. *Forests*, *9*(10), 587. https://doi.org/10.3390/f9100587

Jucker, T., Caspersen, J., Chave, J., Antin, C., Barbier, N., Bongers, F., … Coomes, D. A. (2017). Allometric equations for integrating remote sensing imagery into forest monitoring programmes. *Global Change Biology*, *23*(1), 177–190. https://doi.org/10.1111/gcb.13388

Kachamba, D., Ørka, H., Gobakken, T., Eid, T., & Mwase, W. (2016). Biomass estimation using 3D data from unmanned aerial vehicle imagery in a tropical woodland. *Remote Sensing*, *8*(11), 968. https://doi.org/10.3390/rs8110968

King, D. A. (2005). Linking tree form, allocation and growth with an allometrically explicit model. *Ecological Modelling*, *185*(1), 77–91. https://doi.org/10.1016/j.ecolmodel.2004.11.017

KNMI. (2019). Daggegevens van het weer in Nederland. Retrieved February 21, 2020, from https://projects.knmi.nl/klimatologie/daggegevens/index.cgi

Köhl, M., Magnussen, S., & Marchetti, M. (2006). *Sampling methods, remote sensing and GIS multiresource forest inventory*. Berlin, Heidelberg: Springer. https://doi.org/10.1007/978-3-540-32572-7

Krause, S., Sanders, T. G. M., Mund, J.-P., & Greve, K. (2019). UAV-based photogrammetric tree height measurement for intensive forest monitoring. *Remote Sensing*, *11*(7), 758. https://doi.org/10.3390/rs11070758

Kumar, L., & Mutanga, O. (2017). Remote sensing of above-ground biomass. *Remote Sensing*, *9*(9), 935. https://doi.org/10.3390/rs9090935

Kustiyanto, E. (2019). *Estimating aboveground biomass/carbon stock and carbon sequestration using UAV (Unmanned Aerial Vehicle) in mangrove forest, Mahakam Delta, Indonesia* (Master's Thesis). Retrieved from https://library.itc.utwente.nl/papers_2019/msc/nrm/kustiyanto.pdf

Kwak, D. A., Lee, W. K., Lee, J. H., Biging, G. S., & Gong, P. (2007). Detection of individual trees and estimation of tree height using LiDAR data. *Journal of Forest Research*, *12*(6), 425–434. https://doi.org/10.1007/s10310-007-0041-9

Lehmann, J., Nieberding, F., Prinz, T., & Knoth, C. (2015). Analysis of unmanned aerial system-based CIR images in forestry—A new perspective to monitor pest infestation levels. *Forests*, *6*(12), 594–612. https://doi.org/10.3390/f6030594

Lin, J., Wang, M., Ma, M., & Lin, Y. (2018). Aboveground tree biomass estimation of sparse subalpine coniferous forest with UAV oblique photography. *Remote Sensing*, *10*(11), 1849. https://doi.org/10.3390/rs10111849

Lisein, J., Pierrot-Deseilligny, M., Bonnet, S., & Lejeune, P. (2013). A photogrammetric workflow for the creation of a forest canopy height model from small unmanned aerial system imagery. *Forests*, *4*(4), 922–944. https://doi.org/10.3390/f4040922

López-Serrano, P., López Sánchez, C., Solís-Moreno, R., & Corral-Rivas, J. (2016). Geospatial estimation of above ground forest biomass in the Sierra Madre Occidental in the state of Durango, Mexico. *Forests*, *7*(12), 70. https://doi.org/10.3390/f7030070

Maniatis, D., & Mollicone, D. (2010). Options for sampling and stratification for national forest inventories to implement REDD+ under the UNFCCC. *Carbon Balance and Management*, *5*, 9. https://doi.org/10.1186/1750-0680-5-9

McKendry, P. (2002). Energy production from biomass (part 1): Overview of biomass. *Bioresource Technology*, *83*(1), 37–46. https://doi.org/10.1016/S0960-8524(01)00118-3

McRobert, R. E., & Tomppo, E. O. (2007). Remote sensing support for national forest inventories. *Remote Sensing of Environment*, *110*(4), 412–419. https://doi.org/10.1016/J.RSE.2006.09.034

Messinger, M., Asner, G., & Silman, M. (2016). Rapid assessments of Amazon forest structure and biomass using small unmanned aerial systems. *Remote Sensing*, *8*(8), 615. https://doi.org/10.3390/rs8080615

Mlambo, R., Woodhouse, I., Gerard, F., & Anderson, K. (2017). Structure from motion (SfM) photogrammetry with drone data: A low cost method for monitoring greenhouse gas emissions from forests in developing countries. *Forests*, *8*(3), 68. https://doi.org/10.3390/f8030068

Mohan, M., Silva, C. A., Klauberg, C., Jat, P., Catts, G., Cardil, A., … Dia, M. (2017). Individual tree detection from unmanned aerial vehicle (UAV) derived canopy height model in an open canopy mixed conifer forest. *Forests*, *8*(9), 340. https://doi.org/10.3390/f8090340

Odia, B. E. (2018). *Unmanned aerial vehicle (UAV) datasets for retrieval of forest parameters and estimation of aboveground biomass in Berkelah tropical rainforest, Malaysia* (Master's Thesis). Retrieved from https://library.itc.utwente.nl/login/2018/msc/nrm/odia.pdf

Ota, T., Ogawa, M., Shimizu, K., Kajisa, T., Mizoue, N., Yoshida, S., … Ket, N. (2015). Aboveground biomass estimation using structure from motion approach with aerial photographs in a seasonal tropical forest. *Forests*, *6*(12), 3882–3898. https://doi.org/10.3390/f6113882

Panagiotidis, D., Abdollahnejad, A., Surový, P., & Chiteculo, V. (2017). Determining tree height and crown diameter from high-resolution UAV imagery. *International Journal of Remote Sensing*, *38*(8–10), 2392–2410. https://doi.org/10.1080/01431161.2016.1264028

Pix4D. (2017). *Pix4Dmapper 4.1 user mannual*. Retrieved from https://support.pix4d.com/hc/en-us/articles/204272989-Offline-Getting-Started-and-Manual-pdf

Popescu, S. C. (2007). Estimating biomass of individual pine trees using airborne lidar. *Biomass and Bioenergy*, *31*(9), 646–655. https://doi.org/10.1016/j.biombioe.2007.06.022

Pouliot, D. A., King, D. J., Bell, F. W., & Pitt, D. G. (2002). Automated tree crown detection and delineation in high-resolution digital camera imagery of coniferous forest regeneration. *Remote Sensing of Environment*, *82*(2–3), 322–334. https://doi.org/10.1016/S0034-4257(02)00050-0

Primasatya, R. F., Hussin, Y. A., & Leeuwen, L. M. Van. (2016). *Terrestrial Laser scanning to support carbon estimation in nature conservation area: A case study of Haagse Bos and Snippert Forest, Netherlands*. Paper presented at the 37th Asian Conference on Remote Sensing, ACRS 2016 (pp. 935–944). Colombo, Sri Lanka.

Puliti, S., Ørka, H., Gobakken, T., & Næsset, E. (2015). Inventory of small forest areas using an unmanned aerial system. *Remote Sensing*, *7*(8), 9632–9654. https://doi.org/10.3390/rs70809632

Rodríguez-Veiga, P., Wheeler, J., Louis, V., Tansey, K., & Balzter, H. (2017, March 1). Quantifying forest biomass carbon stocks from space. *Current Forestry Reports*. Springer International Publishing. https://doi.org/10.1007/s40725-017-0052-5

Shah, S. K. (2011). *Modelling the relationship between canopy projection area and above ground carbon stock using high resolution GeoEye satellite images* (Master's Thesis). Retrieved from https://library.itc.utwente.nl/papers_2011/msc/nrm/shah.pdf

Shen, X., Cao, L., Yang, B., Xu, Z., & Wang, G. (2019). Estimation of forest structural attributes using spectral indices and point clouds from UAS-based multispectral and RGB imageries. *Remote Sensing*, *11*(7), 800. https://doi.org/10.3390/rs11070800

Shimano, K. (1997). Analysis of the relationship between DBH and crown projection area using a new model. *Journal of Forest Research*, *2*(4), 237–242. https://doi.org/10.1007/BF02348322

Solberg, S., Astrup, R., Gobakken, T., Næsset, E., & Weydahl, D. J. (2010). Estimating spruce and pine biomass with interferometric X-band SAR. *Remote Sensing of Environment*, *114*(10), 2353–2360. https://doi.org/10.1016/j.rse.2010.05.011

Sterck, F. J., & Bongers, F. (2001). Crown development in tropical rain forest trees: Patterns with tree height and light. *Source: Journal of Ecology*, *89*(1), 1–13. Retrieved from https://www.jstor.org/stable/3072112

Suo, McGovern, & Gilmer. (2019). Coastal dune vegetation mapping using a multispectral sensor mounted on an UAS. *Remote Sensing*, *11*(15), 1814. https://doi.org/10.3390/rs11151814

Thurner, M., Beer, C., Santoro, M., Carvalhais, N., Wutzler, T., Schepaschenko, D., … Schmullius, C. (2014). Carbon stock and density of northern boreal and temperate forests. *Global Ecology and Biogeography*, *23*(3), 297–310. https://doi.org/10.1111/geb.12125

Toochi, E. C. (2018). Carbon sequestration: How much can forestry sequester CO2? *Forestry Research and Engineering: International Journal*, *2*(3). https://doi.org/10.15406/freij.2018.02.00040

Torresan, C., Berton, A., Carotenuto, F., Di Gennaro, S. F., Gioli, B., Matese, A., … Wallace, L. (2017). Forestry applications of UAVs in Europe: A review. *International Journal of Remote Sensing*, *38*(8–10), 2427–2447. https://doi.org/10.1080/01431161.2016.1252477

Tsouros, D. C., Bibi, S., & Sarigiannidis, P. G. (2019). A review on UAV-based applications for precision agriculture. *Information*, *10*(11), 349. https://doi.org/10.3390/info10110349

UNFCCC. (2008). *Kyoto protocol reference manual on accounting of emissions and assigned amount*. Retrieved from https://unfccc.int/resource/docs/publications/08_unfccc_kp_ref_manual.pdf

United Nations. (2015). *Transforming our world: The 2030 agenda for sustainable development*. Retrieved from https://www.unfpa.org/sites/default/files/resource-pdf/Resolution_A_RES_70_1_EN.pdf

Wallace, L., Lucieer, A., Malenovský, Z., Turner, D., & Vopěnka, P. (2016). Assessment of forest structure using two UAV techniques: A comparison of airborne laser scanning and structure from motion (SfM) point clouds. *Forests*, *7*(12), 62. https://doi.org/10.3390/f7030062

Westoby, M. J., Brasington, J., Glasser, N. F., Hambrey, M. J., & Reynolds, J. M. (2012). 'Structure-from-Motion' photogrammetry: A low-cost, effective tool for geoscience applications. *Geomorphology*, *179*, 300–314. https://doi.org/10.1016/J.GEOMORPH.2012.08.021

White, J., Wulder, M., Vastaranta, M., Coops, N., Pitt, D., & Woods, M. (2013). The utility of image-based point clouds for forest inventory: A comparison with airborne laser scanning. *Forests*, *4*(3), 518–536. https://doi.org/10.3390/f4030518

Yin, D., & Wang, L. (2016). How to assess the accuracy of the individual tree-based forest inventory derived from remotely sensed data: A review. *International Journal of Remote Sensing*, *37*(19), 4521–4553. https://doi.org/10.1080/01431161.2016.1214302

Zainuddin, K., Jaffri, M. H., Zainal, M. Z., Ghazali, N., & Samad, A. M. (2016). *Verification test on ability to use low-cost UAV for quantifying tree height.* Paper presented at the 2016 IEEE 12th International Colloquium on Signal Processing and its Applications, CSPA 2016 (pp. 317–321). Institute of Electrical and Electronics Engineers Inc. https://doi.org/10.1109/CSPA.2016.7515853

Zhang, J., Hu, J., Lian, J., Fan, Z., Ouyang, X., & Ye, W. (2016). Seeing the forest from drones: Testing the potential of lightweight drones as a tool for long-term forest monitoring. *Biological Conservation*, *198*, 60–69. https://doi.org/10.1016/j.biocon.2016.03.027

Zhao, K., Popescu, S., & Nelson, R. (2009). Lidar remote sensing of forest biomass: A scale-invariant estimation approach using airborne lasers. *Remote Sensing of Environment*, *113*(1), 182–196. https://doi.org/10.1016/j.rse.2008.09.009

Zhu, X., & Liu, D. (2015). Improving forest aboveground biomass estimation using seasonal Landsat NDVI time-series. *ISPRS Journal of Photogrammetry and Remote Sensing*, *102*, 222–231. https://doi.org/10.1016/j.isprsjprs.2014.08.014

APPENDICES

Appendix 1. Descriptive statistics of plot-wise field data.

Plot	Diameter at breast height (cm)				Tree height (m)			
	Mean	Min	Max	SD	Mean	Min	Max	SD
1	31.50	14.00	53.00	12.17	21.50	12.00	31.00	6.11
2	31.35	17.00	49.00	11.73	22.29	13.00	29.00	4.59
3	33.45	12.00	61.00	13.84	24.90	12.00	32.00	5.81
4	33.48	23.00	41.00	5.17	22.95	20.00	26.00	1.69
5	37.71	33.00	48.00	4.92	24.71	22.00	28.00	1.77
6	39.69	12.00	51.00	8.61	27.69	11.00	33.00	5.04
7	28.91	12.00	41.00	6.38	20.64	14.00	24.00	2.32
8	33.06	12.00	53.00	10.44	22.72	16.00	32.00	3.91
9	31.56	14.00	44.00	7.61	22.94	16.00	27.00	3.04
10	28.44	19.00	39.00	5.98	20.50	16.00	23.00	1.82
11	30.81	14.00	40.00	5.56	22.05	15.00	27.00	2.48
12	35.87	26.00	46.00	5.38	22.93	19.00	25.00	1.75
13	41.82	17.00	56.00	12.94	27.45	16.00	31.00	5.50
14	38.15	17.00	52.00	9.53	23.69	6.00	29.00	5.78
15	25.38	12.00	37.00	7.81	18.04	11.00	23.00	3.71
16	28.21	12.00	47.00	11.83	18.37	6.00	25.00	4.99
17	19.94	12.00	28.00	3.33	21.00	17.00	24.00	1.67
18	29.79	19.00	38.00	5.34	19.89	14.00	23.00	2.16
19	25.58	17.00	39.00	4.91	21.79	18.00	24.00	1.77
20	22.29	11.00	32.00	5.45	17.32	12.00	21.00	2.50
21	23.53	11.00	38.00	5.89	18.03	11.00	22.00	2.53
22	28.36	14.00	42.00	7.55	19.64	11.00	26.00	4.63
23	21.64	12.00	31.00	5.26	17.86	12.00	22.00	2.09
24	25.89	15.00	40.00	6.67	18.94	14.00	23.00	2.24
25	29.67	12.00	54.00	11.69	21.14	15.00	26.00	2.83
26	26.30	11.00	42.00	9.50	16.90	11.00	22.00	2.85
27	28.70	12.00	42.00	7.54	19.20	10.00	24.00	2.97
28	39.13	12.00	52.00	13.24	23.60	10.00	35.00	7.13
29	38.55	18.00	53.00	10.40	21.82	13.00	28.00	4.12
30	39.94	19.00	57.00	9.78	25.12	11.00	33.00	6.48
31	42.13	31.00	56.00	9.16	27.88	23.00	31.00	3.14
32	37.47	12.00	57.00	12.67	23.13	9.00	30.00	5.77
33	31.06	13.00	59.00	13.62	21.29	12.00	30.00	5.80
34	32.71	12.00	44.00	11.41	22.29	10.00	26.00	5.57
35	27.00	15.00	40.00	7.42	20.88	11.00	29.00	3.81

Appendix 2. Plot-wise tree species distribution.

Plot	Norway spruce	Scots pine	Douglas-fir	Larix decidua	Total
1	2		14		16
2	8	2	7		17
3			20		20
4	21				21
5	14				14
6	16				16
7	22				22
8	14		3	1	18
9	16				16
10	17			1	18
11	21				21
12	9			6	15
13			11		11
14	1	12			13
15	23	1			24
16	5		5	9	19
17				36	36
18	19				19
19	24				24
20	26	2			28
21	30				30
22	7			4	11
23	28				28
24	18				18
25	3	12	6		21
26	19			1	20
27	20				20
28	5	6	3	1	15
29	4	7			11
30	5	12			17
31		8			8
32	4	11			15
33	10	7			17
34	8			6	14
35	6	3	3	5	17
Total	425	83	72	70	650

Appendix 3. Summary of result from processed UAV images extracted from the quality report generated by Pix4Dmapper.

	Multispectral	RGB
Summary		
Average GSD	10.69 cm	4.70 cm
Total area	48.71 ha	52.65 ha
Time for initial processing	01hr:13m:56s	01h:19m:37s
Quality check		
Dataset	3636 out of 3692 images (98%) calibrated	1203 out of 1206 images (99%) calibrated
Georeferencing RMSE	7 GCPs, RMSE = 0.041 m	6 GCPs, RMSE = 0.047 m
Bundle Block Adjustment		
Mean reprojection error (pixels)	0.14	0.12
Geolocation		
GCP RMSE (m)	x = 0.013; y = 0.009; z = 0.104	x = 0.022; y = 0.030; z = 0.094
Check point RMSE (m)	x = 0.016; y = 0.065; z = 0.219	x = 0.044; y = 0.040; z = 0.393
Coordinate Systems		
Image coordinate system	WGS 84	WGS 84
GCP & output coordinate system	Amersfoort/ RD New	Amersfoort/ RD New
Point Cloud Densification		
Number of 3D densified points	5,631,379	61,116,170
Average point cloud density (m^{-3})	2.61	30.92
Time for point cloud densification	17m:53s	05hr:53m:36s
DSM, Orthomosaic, and DTM		
DSM and orthomosaic resolution	1*GSD (10.7 [cm/pixel])	1*GSD (4.7 [cm/pixel])
DTM resolution	5*GSD (10.7 [cm/pixel])	5*GSD (4.7 [cm/pixel])
Time for DSM generation	05m:53s	50m:46s
Time for orthomosaic generation	55m:26s	03hr:34m:47s
Time for DTM generation	01m:00s	07m:06s

Appendix 4. Model development and validation summary.

MS model development

Model	Predictor (x)	Equation	R^2	RMSE	RMSE (%)	Bias	Bias (%)
Linear	TH	y = 2.2676x - 15.546	0.589	6.428	21.168	0.001	0.002
Linear	CPA	y = 0.6982x + 18.027	0.696	5.526	18.199	0.000	0.001
Linear	CD	y = 10.924x + 5.9376	0.744	5.070	16.695	0.001	0.003
Linear	TH x CD	y = 0.4034x + 11.447	0.825	4.198	13.823	-0.002	-0.008
Log	TH x CD	y = 17.418ln(x) - 34.542	0.799	4.489	14.784	0.001	0.004
Power	TH x CD	$y = 2.9262x^{0.6127}$	0.843	4.016	13.225	-0.284	-0.934
Quadratic	TH x CD	$y = -0.0019x^2 + 0.6219x + 6.3708$	0.847	3.918	12.902	0.026	0.085

MS model validation

Model	R^2	Equation	S	RMSE	RMSE (%)	Bias	Bias (%)
Power	0.815	$y = 2.9262x^{0.6127}$	4.394	4.396	14.406	-0.092	-0.301
Quadratic	0.821	$y = -0.0019x^2 + 0.6219x + 6.3708$	4.333	4.361	14.291	0.244	0.801

RGB model development

Model	Predictor (x)	Equation	R^2	RMSE	RMSE (%)	Bias	Bias (%)
Linear	TH	y = 2.1093x - 16.195	0.629	6.108	20.115	-0.001	-0.003
Linear	CPA	y = 0.6883x + 17.732	0.695	5.535	18.228	0.001	0.002
Linear	CD	y = 11.164x + 4.8064	0.749	5.023	16.542	-0.001	-0.003
Linear	TH x CD	y = 0.36x + 11.458	0.804	4.437	14.613	0.002	0.005
Log	TH x CD	y = 17.655ln(x) - 37.492	0.795	4.541	14.955	0.001	0.005
Power	TH x CD	$y = 2.5981x^{0.6249}$	0.849	4.194	13.812	-0.283	-0.931
Quadratic	TH x CD	$y = -0.0018x^2 + 0.5871x + 5.4961$	0.834	4.082	13.441	-0.117	-0.384

RGB model validation

Model	R^2	Equation	S	RMSE	RMSE (%)	Bias	Bias (%)
Power	0.795	$y = 2.5981x^{0.6249}$	4.625	4.654	15.251	-0.048	-0.157
Quadratic	0.805	$y = -0.0018x^2 + 0.5871x + 5.4961$	4.520	4.537	14.869	0.076	0.247

Appendix 5. Plot level AGB and extrapolated hectare level AGB.

Plot	Field AGB (Mg plot^{-1})	MS AGB (Mg plot^{-1})	RGB AGB (Mg plot^{-1})	Field AGB (Mg ha^{-1})	MS AGB (Mg ha^{-1})	RGB AGB (Mg ha^{-1})
1	14.72	14.49	14.84	294.49	289.73	296.85
2	11.45	11.61	11.55	228.93	232.15	231.09
3	23.50	22.02	22.47	469.93	440.37	449.34
4	9.74	8.20	11.16	194.76	163.95	223.25
5	8.40	10.00	9.83	167.99	200.07	196.67
6	11.60	12.82	13.52	232.03	256.30	270.35
7	6.98	7.20	8.13	139.57	143.90	162.51
8	12.32	14.44	15.85	246.36	288.88	317.06
9	6.82	8.26	9.18	136.37	165.21	183.58
10	5.94	6.18	7.01	118.85	123.68	140.28
11	8.60	8.85	10.95	172.03	177.01	219.08
12	7.45	8.18	8.28	149.09	163.57	165.55
13	20.08	21.02	20.55	401.51	420.49	410.97
14	7.55	8.28	8.82	151.03	165.66	176.41
15	6.17	6.04	6.85	123.33	120.84	136.98
16	10.81	10.89	10.85	216.25	217.84	217.01
17	4.81	7.57	7.78	96.24	151.48	155.68
18	6.10	6.60	7.07	122.02	132.00	141.34
19	6.50	7.03	7.35	129.97	140.67	147.00
20	4.92	4.65	5.10	98.47	93.03	101.94
21	6.06	5.92	6.61	121.15	118.41	132.25
22	3.19	3.68	4.08	63.78	73.65	81.69
23	4.80	4.39	5.04	96.04	87.78	100.81
24	4.74	4.29	4.51	94.79	85.77	90.25
25	10.14	10.16	10.28	202.79	203.18	205.53
26	4.80	4.17	4.57	96.09	83.44	91.31
27	5.91	5.80	6.34	118.11	115.95	126.75
28	13.01	13.33	12.70	260.22	266.55	254.05
29	6.19	5.07	4.58	123.86	101.43	91.64
30	10.63	8.43	8.17	212.52	168.57	163.35
31	5.62	4.62	4.09	112.46	92.37	81.88
32	8.85	8.06	7.89	177.05	161.24	157.75
33	7.06	6.55	6.11	141.26	130.93	122.28
34	6.38	7.11	7.23	127.57	142.12	144.65
35	5.36	7.75	7.82	107.25	154.96	156.37
Sum	**297.21**	**303.66**	**317.17**	**5944.15**	**6073.19**	**6343.49**
Mean	**8.49**	**8.68**	**9.06**	**169.83**	**173.52**	**181.24**

Appendix 6. Plot level AGC and extrapolated hectare level AGC.

Plot	Field AGC (Mg plot^{-1})	MS AGC (Mg plot^{-1})	RGB AGC (Mg plot^{-1})	Field AGC (Mg ha^{-1})	MS AGC (Mg ha^{-1})	RGB AGC (Mg ha^{-1})
1	7.36	7.24	7.42	147.24	144.87	148.42
2	5.72	5.80	5.78	114.46	116.07	115.54
3	11.75	11.01	11.23	234.97	220.19	224.67
4	4.87	4.10	5.58	97.38	81.98	111.62
5	4.20	5.00	4.92	84.00	100.04	98.33
6	5.80	6.41	6.76	116.01	128.15	135.17
7	3.49	3.60	4.06	69.78	71.95	81.25
8	6.16	7.22	7.93	123.18	144.44	158.53
9	3.41	4.13	4.59	68.19	82.60	91.79
10	2.97	3.09	3.51	59.43	61.84	70.14
11	4.30	4.43	5.48	86.01	88.50	109.54
12	3.73	4.09	4.14	74.54	81.78	82.77
13	10.04	10.51	10.27	200.75	210.25	205.49
14	3.78	4.14	4.41	75.52	82.83	88.21
15	3.08	3.02	3.42	61.66	60.42	68.49
16	5.41	5.45	5.43	108.13	108.92	108.50
17	2.41	3.79	3.89	48.12	75.74	77.84
18	3.05	3.30	3.53	61.01	66.00	70.67
19	3.25	3.52	3.67	64.98	70.34	73.50
20	2.46	2.33	2.55	49.24	46.51	50.97
21	3.03	2.96	3.31	60.58	59.21	66.12
22	1.59	1.84	2.04	31.89	36.83	40.84
23	2.40	2.19	2.52	48.02	43.89	50.40
24	2.37	2.14	2.26	47.39	42.88	45.13
25	5.07	5.08	5.14	101.40	101.59	102.77
26	2.40	2.09	2.28	48.04	41.72	45.66
27	2.95	2.90	3.17	59.06	57.98	63.38
28	6.51	6.66	6.35	130.11	133.27	127.03
29	3.10	2.54	2.29	61.93	50.71	45.82
30	5.31	4.21	4.08	106.26	84.28	81.67
31	2.81	2.31	2.05	56.23	46.18	40.94
32	4.43	4.03	3.94	88.52	80.62	78.87
33	3.53	3.27	3.06	70.63	65.46	61.14
34	3.19	3.55	3.62	63.78	71.06	72.32
35	2.68	3.87	3.91	53.62	77.48	78.19
Sum	**148.60**	**151.83**	**158.59**	**2972.08**	**3036.59**	**3171.75**
Mean	**4.25**	**4.34**	**4.53**	**84.92**	**86.76**	**90.62**

Appendix 7. Field data collection sheet.

Field data sheet

Name of recorder ……………………… Date (dd/mm/yy) ………… Plot size radius (m) …….

Plot no.	Coordinate of plot centre		Elevation (m)
	X:	Y:	

Tree no.	Species	DBH (cm)	Height (m)	Distance from PC (m)	Bearing from PC (degree)	Remarks
1						
2						
3						
4						
5						
6						
7						
8						
9						
10						
11						
12						
13						
14						
15						
16						
17						
18						
19						
20						
21						
22						
23						
24						
25						
26						
27						
28						
29						
30						